An optimal stress jump interface condition for the fluid-porous multi-dimensional flow

Philippe Angot, Benoît Goyeau, J. Alberto Ochoa-Tapia

Transport in Porous Media manuscript No.
(will be inserted by the editor)

An optimal stress jump interface condition for the fluid-porous multi-dimensional flow

Philippe Angot · Benoît Goyeau · J. Alberto Ochoa-Tapia

Received: February 26, 2021 / Accepted: date

Abstract In this study, we present and discuss several original sets of jump interface conditions for the coupling of multi-dimensional models in fluid-porous systems with arbitrary flow directions. There are issued from the theoretical derivation carried out in Angot et al. (2017) using the generalized Darcy-Brinkman equation in the free flow/porous medium inter-region Ω_{fp} and a suitable asymptotic analysis for the dimensional reduction to a dividing surface Σ between the free-fluid Ω_f and porous Ω_p regions. The macroscale models can be either the Stokes/Darcy or Stokes/Darcy-Brinkman coupled problems in the fluid-porous systems, so covering the whole range of porosity $0 < \phi_p < 1$ of the permeable medium. All sets of boundary conditions include jumps of tangential velocity vector and/or stress vector either at the top surface Σ_t or at the bottom surface Σ_b of a transition layer Ω_{fp}. Besides, in all the latter jump conditions, the inherent tensorial form of the stress jump condition ensures to handle flows over anisotropic porous media. In the present study, all these interface conditions are validated and calibrated against three benchmark problems including pressure-driven or shear-driven flows. The reference solution is obtained by the numerical solution of the single-domain continuum model computed by a second-order finite volume method. This allows us to calibrate the slip velocity α_Σ and stress jump friction β_Σ coefficients that must be non negative to ensure the mechanical energy dissipation. Then, it is proposed for both the Stokes/Darcy-Brinkman and Stokes/Darcy coupled problems, an optimally accurate stress jump interface condition associated to the

Philippe Angot
Aix-Marseille Université
Institut de Mathématiques de Marseille, CNRS UMR-7373, Centrale Marseille,
39 rue F. Joliot-Curie, 13453 Marseille cedex 13, France
E-mail: *philippe.angot@univ-amu.fr*

Benoît Goyeau
Ecole Centrale-Supélec, Université Paris-Saclay, EM2C, CNRS UPR-288,
8-10 rue Joliot-Curie, 91190 Gif-sur-Yvette, France

J. Alberto Ochoa-Tapia
Universidad Autónoma Metropolitana-Iztapalapa, Departamento de Ingeniería de Procesos e Hidráulica,
Mexico 09340 D.F., Mexico

velocity continuity on a suitable dividing surface $\Sigma = \Sigma_b$, that minimizes the loss of flow rate. The comparative performance results clearly indicate that the latter interface condition on Σ_b tremendously outperforms all the others. Moreover, all the related coupled problems are shown to be globally dissipative over the full range of porosity which ensures their mathematical (at least formally) and physical stability.

Keywords Fluid-porous systems · Multi-dimensional viscous flows · Stokes/Darcy-Brinkman model · Stokes/Darcy model · Optimal stress jump interface condition · Global dissipation of mechanical energy

PACS

Mathematics Subject Classification (2010) 76D07 · 76S05

Article Highlights

- Two sets of jump conditions issued from our recent derivations are investigated and compared with others from the literature to couple the Stokes/Darcy-Brinkman or Stokes/Darcy models for the multi-directional fluid-porous flows.
- All the sets applied either at the top or at the bottom surface of the inter-region are discussed and shown to ensure the global dissipation of mechanical energy for the three-dimensional flows with no restriction on the size of the data.
- The calibration against three pressure-driven and shear-driven benchmarks shows that the set of stress jump conditions with velocity continuity is optimal for each model to minimize the loss of flow rate in the viscous boundary layer.

1 Main objectives and highlights

1.1 Introduction

The issue of accurately describing the mass, momentum transport, flow structure and transfer phenomena through and over a permeable region is a fundamental transport problem. Indeed, most of the coupled phenomena (heat transfer, diffusion-dispersion of a contaminant, mixing and reaction-diffusion) depend in a crucial way on the inter-region transport. Moreover, this topic has a broad range of applications in many fields of Physics (colloidal particles), biomechanics systems and microbiological processes (bone growth, biofilms, cell proliferation), microfluidics and medical applications, industrial engineering (dendritic solidification of multi-component mixtures, filtration processes, oil recovery, separation processes, insulation materials, risk assessment for nuclear waste storage). This is also present in a large variety of Geophysics systems, environmental situations or water resources systems (surface water-groundwater interactions, hydrology, geothermal energy recovery, sea water intrusion, mid-ocean ridges, interaction between atmosphere and vegetation canopy, benthic boundary layers). For example, we refer to Finnigan (2000); Koch and Hill (2001); Nepf (2012); Monti et al. (2019); Nield and Bejan (2017); Bottaro (2019); Zampogna et al. (2019); Parasyris et al. (2020) and the references therein for many examples of application.

However, due to the large difference of the characteristic length scales involved in these heterogeneous configurations, from the local pore scale size to the macroscale length, the computation of pore-scale solutions to accurately describe the transfer phenomena at all scales is not affordable. Indeed, transfer problems in porous media for real-world applications span a very wide range of physical length scales: from micrometer up to the km scale, while the time scales vary from seconds to several months or years. Hence, as made for turbulence modelling, the momentum transport analysis is often performed at the macroscopic scale using suitable averaging and local deviations filtering. So, the derivation of such reliable and fully justified macroscale models is required to tackle fundamental studies at a fluid-porous interface (stability, boundary layer, multiphase flows, turbulence) and to deal with the large variety of applications foregoing mentioned. If the macroscale flow models inside porous media are nowdays well-established, e.g. Dullien (1992); Nield and Bejan (2017), this is not the case of the jump boundary conditions that should be used to accurately couple the macroscale fluid-porous models. Indeed, the concept of dividing surface is actually closely related to the nature of the average representation at the interfacial region.

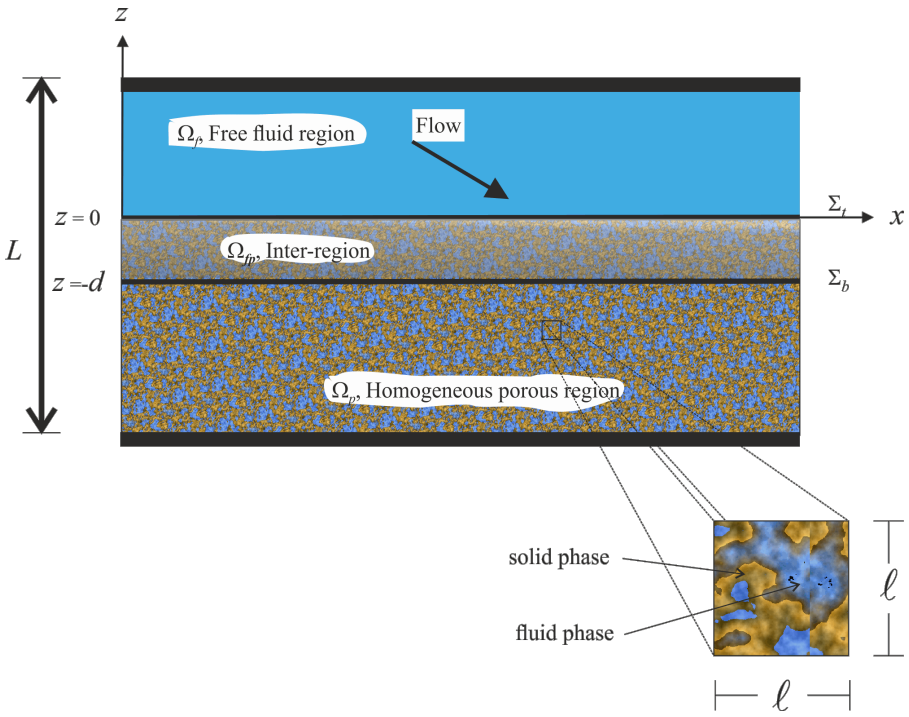

Fig. 1 Configuration of the single-domain continuum modelling for an arbitrary flow direction: thin transition porous layer Ω_{fp} of thickness $d \ll L$ with evolving heterogeneity and continuous inter-region with both the free-fluid domain Ω_f and porous domain Ω_p including a zoom of microstructure in a representative unit cell of size ℓ.

Therefore, the works related to transport in fluid-porous flows mainly deal with two approaches: the single-domain (or one-domain) continuum modelling and the two-domain modelling that are obviously connected to each other. The one-domain continuum modelling for the fluid-porous viscous flow originates from Brinkman's equation (Brinkman 1947a,b) to connect the Stokes equation with Darcy's law (Darcy 1856), who early introduces the notions of effective viscosity in a porous medium and viscous boundary layer. He is then followed by many authors. Among them and following the ideas of Neale and Nader (1974) and Whitaker (1969) with the volume averaging method, Ross (1983) early introduced the concept of a fluid/porous medium inter-region Ω_{fp} between the pure fluid domain Ω_f and the homogeneous porous medium one Ω_p (see figure 1). He derived the momentum equation governing the creeping flow inside Ω_{fp} as an alternative to the two-domain approach of Beavers and Joseph (1967).

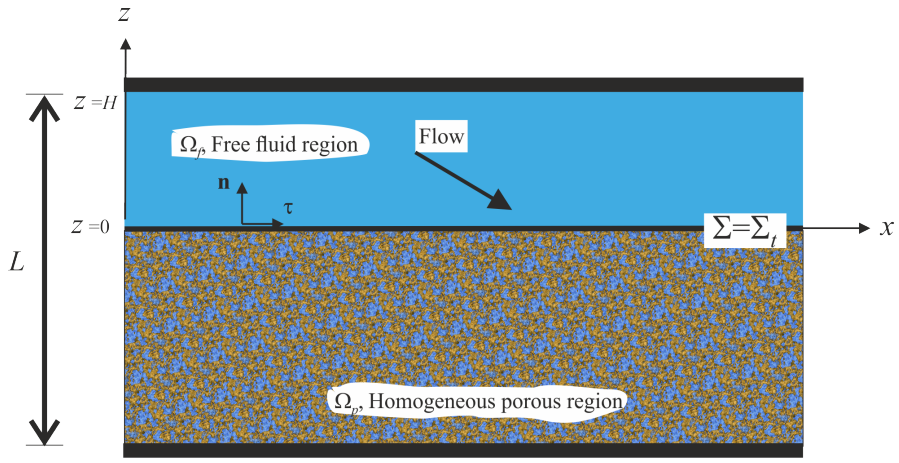

Fig. 2 Configuration of the two-domain modelling: thin transition layer Ω_{fp} dimensionally reduced to a sharp dividing surface $\Sigma = \Sigma_\xi$ located at $z_\Sigma = -d + (1-\xi)d$ with $\xi := |z_\Sigma|/d$ and $0 \le \xi \le 1$. Here, the usual choice is represented with $\Sigma = \Sigma_t$ located at the top $z = 0$ of Ω_{fp}.

The two-domain modelling introducing a dividing surface Σ (see figure 2)[1] associated to suitable jump conditions dates back to Beavers and Joseph (1967) who take Σ at the top surface of the porous medium considered as tangent to the upper row of solid inclusions facing the free fluid. They heuristically introduce a velocity-slip interface condition for the 1-D Poiseuille channel flow parallel to the porous layer of which the flow is governed by Darcy's law. Their semi-empirical condition was supported by experimental results. This condition was later completed by Jones (1973) symmetrizing the fluid stress by considering the full stress tensor. It was also justified and simplified by Saffman (1971) neglecting the filtration velocity with respect to the

[1] The reader should be careful that the notations of Ω_f and Ω_p are not obviously consistent between figure 1 and figure 2, but this is for the practical sake of simplicity and convenience. Indeed, the layer Ω_{fp} is occupied (or partially occupied) by the pure fluid or the porous medium in the two-domain representations of figures 2 or 3.

fluid velocity at the dividing surface, so eliminating the explicit jump in the interface relation. An investigation of the influence of interface location for Beavers-Joseph's condition is made heuristically by several authors, e.g. LeBars and Worster (2006); Zampogna and Bottaro (2016); see also Nield (1983, 2000, 2009) and Auriault (2010).

Further, Ochoa-Tapia and Whitaker (1995a,b) derived a shear stress jump condition by volume averaging for the same 1-D configuration, but when the flow in the porous medium is governed by the Darcy-Brinkman equation with an effective viscosity $\widetilde{\mu}$ (or μ_{eff}) $= \mu/\phi_p$ in the porous medium (see also Lundgren (1972); Prieur du Plessis and Masliyah (1988)), μ being the dynamic viscosity of the fluid, ϕ_p the porosity (or volume fraction of pore). By considering the Taylor brush configuration, Duman and Shavit (2009) investigated the sensitivity of the shear-stress jump condition to the dividing surface location. In the same conditions, but without imposing the continuity of the streamwise velocity made in the previous derivation, Valdés-Parada et al. (2013) derived two jump boundary conditions for the tangential velocity and shear stress, respectively. Using phenomenological thermodynamics of mixtures, Cieszko and Kubik (1999); Kubik and Cieszko (2005) early derived a set of interface conditions including also the jumps of both tangential velocity and shear stress.

We refer to Angot et al. (2017) which provides a more comprehensive synthesis of the works for the 1-D non-inertial creeping flow parallel to the porous layer made by upscaling procedures, two-scale homogenization Hornung (1997); Auriault et al. (2009) or volume averaging Whitaker (1999), as well as experimental and computational studies of validation. For the case of inertial laminar flows, we refer to our recent study Angot et al. (2021) which derives original nonlinear jump interface conditions for arbitrary flow directions.

1.2 State of the art on interface conditions for fluid-porous flow models

As described in section 1.1 and Angot et al. (2017), most of the interface conditions related to the two-domain modelling with a dividing surface for the creeping flow are now well-established for the 1-D channel or shear flow parallel to the porous bed, either with the Stokes/Darcy model Beavers and Joseph (1967); Saffman (1971); Jones (1973); LeBars and Worster (2006) or with the Stokes/Darcy-Brinkman model Ochoa-Tapia and Whitaker (1995a,b); Cieszko and Kubik (1999); Kubik and Cieszko (2005); Valdés-Parada et al. (2013). Nevertheless, for the needs of calculations of 2-D/3-D flows to solve real world problems and simulate applications, many authors use a set of interface conditions that are extended *ad hoc* from the original ones with no justification. For example, let us consider the coupling of the Stokes/Darcy problem (1) below with usual notations that is many times studied in the literature, where K_p is the permeability of the isotropic and homogeneous porous region Ω_p:

$$\begin{cases} \boldsymbol{\nabla}\cdot\mathbf{v} = 0 & \text{in } \Omega_f \cup \Omega_p, \\ -\mu\Delta\mathbf{v} + \nabla p = \rho\boldsymbol{f} & \text{in } \Omega_f, \\ \mu K_p^{-1}\mathbf{v} + \nabla p = \rho\boldsymbol{f} & \text{in } \Omega_p. \end{cases} \tag{1}$$

Then, with the dividing surface $\Sigma = \Sigma_t$ (see figure 2) originally chosen at the top surface of the transition layer Ω_{fp}, almost all authors use the set of boundary conditions below

inherited from the original Beavers-Joseph-Jones condition (Beavers and Joseph 1967; Jones 1973) introducing the dimensionless velocity-slip coefficient $\alpha_{\rm bj}$ at the interface:

$$\begin{cases} [\![\mathbf{v}\cdot\boldsymbol{n}]\!]_\Sigma = 0 \\ \boldsymbol{\tau}_j\cdot\left(\nabla\mathbf{v}+\nabla\mathbf{v}^T\right)_\Sigma\cdot\boldsymbol{n} = \dfrac{\alpha_{\rm bj}}{\sqrt{K_p}}[\![\mathbf{v}\cdot\boldsymbol{\tau}_j]\!]_\Sigma, \quad \text{for } j=1,2 \qquad \text{on } \Sigma=\Sigma_t. \\ \boldsymbol{n}\cdot[\![\boldsymbol{\sigma}(\mathbf{v},p)\cdot\boldsymbol{n}]\!]_\Sigma = 0 \end{cases} \tag{2}$$

In (2), the Cauchy stress vector $\boldsymbol{\sigma}(\mathbf{v},p)\cdot\boldsymbol{n}$ is defined as: $\boldsymbol{\sigma}^f(\mathbf{v},p)\cdot\boldsymbol{n} := \mu(\nabla\mathbf{v}+\nabla\mathbf{v}^T)^f\cdot\boldsymbol{n} - p^f\boldsymbol{n}$[2] in the free-fluid region and $\boldsymbol{\sigma}^p(\mathbf{v},p)\cdot\boldsymbol{n} := -p^p\boldsymbol{n}$ in the porous bulk. The jump quantity $[\![.]\!]_\Sigma$ on Σ is oriented by the unit normal vector $\boldsymbol{n}$ on Σ (directed arbitrarily outwards of the porous region in figure 2). The couple of vectors $(\boldsymbol{\tau}_1,\boldsymbol{\tau}_2)$ denotes a local basis of tangential vectors on the surface Σ. Then, it should be noticed that the first condition in (2), justified by the authors as the mass conservation at the interface for an incompressible flow, is only a first-order approximation in $O(d/L)$ (d being the thickness of Ω_{fp}, L the macroscale length) as early shown by Ene and Sanchez-Palencia (1975); Lévy and Sanchez-Palencia (1975) and more recently by Angot et al. (2017). Indeed, for the dimensional reduction of fractures in porous media using the asymptotic analysis of thin layers, a higher-order approximation is required to get an effective flow along the fractures as carried out Angot (2003); Angot et al. (2005, 2009). More importantly, the last condition in (2) meaning the continuity of the normal stress and generally justified as the balance of normal forces at the dividing surface, is problematic. As shown in (Angot et al. 2017, section III.D) by asymptotic analysis in Ω_{fp} and recalled in (Angot et al. 2021, Eqs (18) using Remark 3), the conditions (2) should be replaced by a generalized set precised later in Section 2.2 using (Angot et al. 2017, sections III.D.2 & III.D.3) that includes an additional stress-jump condition. In these generalized velocity and stress jump conditions, a tensor quantity $\boldsymbol{\beta}_\Sigma$ is defined with an effective permeability tensor on Σ as the dimensionless friction tensor at the dividing surface and it is obtained by averaging Darcy's drag inside Ω_{fp}. Then it appears, by considering no stress jump at the interface like in (2), that the effective Darcy friction on Σ should be neglected. However, this amounts to neglect Darcy's drag force inside the transition layer or viscous boundary layer that is not physically relevant since this region is occupied by an heterogeneous porous medium and the terms have the same order of magnitude as shown in (Angot 2018, Remark 2.2). This is also in agreement with the theoretical derivations of Minale (2014a,b) for the 1-D shear flow in fluid-porous layers. Moreover, this is also confirmed by the recent paper Eggenweiler and Rybak (2021), using two-scale homogenization to generalize the works of Jäger and Mikelić (2000, 2009); Carraro et al. (2013, 2015) for the two-dimensional case with arbitrary flow directions, who obtain a set of interface conditions similar to ours in Section 2.2. A recent study Lācis et al. (2020), using a different approach than Eggenweiler and Rybak (2021), also proposes a generalization of these latter works giving a form of interface conditions similar to our set. Another obvious drawback of (2) lies in the fact that, the coefficient $\alpha_{\rm bj}$ being a scalar quantity only, Eqs (2) are not adequate to model anisotropic flow configurations. Some

[2] The notation := is used in order to specify that the equality is considered as a definition.

authors nonetheless have tried to consider α_{bj} as a tensorial quantity and to calibrate its coefficients by fitting with numerical results, but this seems unsatisfactory. Above all, this is in contradiction with the general derivation of the second equation in (2) carried out by asymptotic analysis in (Angot et al. 2017, section III.B.2). It clearly appears indeed that this equation comes from averaging the definition of the stress vector $\boldsymbol{\sigma}(\mathbf{v},p)\cdot\boldsymbol{n}$ over Ω_{fp} and that the multiplicative coefficient in front of $[\![\mathbf{v}]\!]_\Sigma$ is only a scalar one, equal for all components, and cannot be a full tensor. Moreover, this is confirmed by the recent numerical experiments made in Eggenweiler and Rybak (2020) that conclude that the set of interface conditions (2) is unsuitable to correctly and accurately represent anisotropic flow configurations.

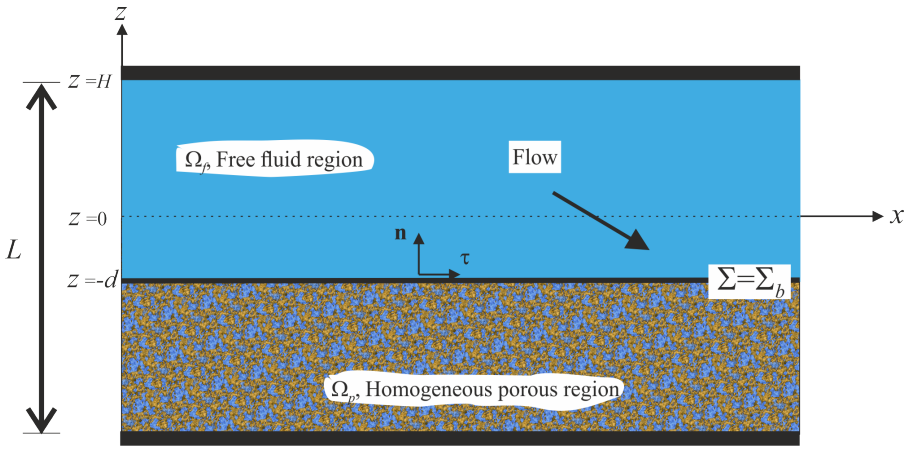

Fig. 3 Configuration of the two-domain modelling: thin transition layer Ω_{fp} dimensionally reduced to a sharp dividing surface $\Sigma=\Sigma_\xi$ located at $z_\Sigma=-d+(1-\xi)d$ with $\xi:=|z_\Sigma|/d$ and $0\le\xi\le 1$. Here, a new choice is considered with $\Sigma=\Sigma_b$ located at the bottom $z=-d$ of Ω_{fp}.

That is the reason why a comprehensive set of jump interface conditions parametrized by the location ξ of the dividing surface Σ inside Ω_{fp} (see figures 2 and 3) is derived in Angot et al. (2017) by asymptotic theory and summarized in (Angot et al. 2021, Eqs (17,18,34) using Remark 3). In the more general case, these conditions include jumps of both the tangential velocity and stress vectors. It is shown that they are suitable generalizations, for the multi-dimensional creeping flow with arbitrary flow directions, of all the known interface conditions developed for the 1-D channel flow parallel to the porous layer, namely Beavers and Joseph (1967); Ochoa-Tapia and Whitaker (1995a,b); Valdés-Parada et al. (2013). Besides, they have been developed to couple both the Stokes/Darcy-Brinkman and Stokes/Darcy problems, just by changing the definition of the related stress vector $\boldsymbol{\sigma}^p(\mathbf{v},p)\cdot\boldsymbol{n}$ in the porous region Ω_p. Let us mention that similar jump interface conditions as those derived in Angot et al. (2017), the so-called jump embedded boundary conditions (JEBC), are early devised in Angot (2010, 2011) on the basis of mathematical analysis to generalize for vector problems the JEBC for scalar interface models of diffusion problems introduced in Angot (2003, 2005). Moreover in Angot (2018), the coupled Stokes/Darcy-Brinkman and

Stokes/Darcy unsteady problems endowed with their related set of jump interface conditions derived in Angot et al. (2017) are both proved to be globally well-posed in time with no restriction on the size of the data. In particular, this holds true whatever the size of the velocity-slip coefficient $\alpha_\Sigma > 0$ for the Stokes/Darcy problem, giving so a solution to some mathematical issues due to the full Beavers-Joseph jump condition. Indeed, the traces of weak solutions in the porous region are not generally strong enough for its tangential component to be well defined.

1.3 Objectives and highlights of the present study

In the present work, it is shown that other sets of jump boundary conditions than those usually found in the literature can be used to couple the Stokes/Darcy-Brinkman and Stokes/Darcy problem as a by-product of the derivation made in Angot et al. (2017) when the interface is chosen at the bottom surface of Ω_{fp}, *i.e.* $\Sigma = \Sigma_b$ located at $\xi = 1$ as shown in figure 3. In particular and thanks to the lower position of the dividing surface, the coupling conditions reduce to a stress-jump condition with no jump of velocity for the Stokes/Darcy and Stokes/Darcy-Brinkman problems. Then, the main objectives is to validate, calibrate and compare the newly proposed sets of jump interface conditions on Σ_t or Σ_b. The coupling of both the Stokes/Darcy and Stokes/Darcy-Brinkman macroscale models, generally treated separately in the literature, are here considered within the same unified setting in order to cover the full porosity range $0 < \phi_p < 1$ of the permeable medium. All the jump interface conditions are shown to fulfill the dissipation of total energy which ensures in particular that the static equilibrium is always reached with a vanishing velocity whatever the considered model. Moreover, an original procedure of selection of the best interface conditions among all possible calibration solutions satisfying $\alpha_\Sigma \geq 0$ and $\beta_\Sigma \geq 0$ to ensure the global dissipation is proposed. The results clearly show that the optimal set of stress jump conditions with no velocity slip yields the best solution to minimize the loss of volumic flow rate.

The paper is organized as follows. Section 2 details the general asymptotic interface model and discusses the particular sets of jump interface conditions obtained when the dividing surface is chosen at Σ_t or Σ_b. The mechanical energy balance is derived in Section 3 and the dissipation of total energy is studied. In Section 4, the jump interface conditions are validated, calibrated and compared against the numerical solutions of the single-domain continuum model for three flow benchmark problems at a permeable interface. A summary of the best results is supplied in Section 4.5. In the last Section 5, some concluding remarks and perspectives are drawn.

2 Original jump interface conditions for arbitrary flow directions

For the incompressible creeping viscous flow inside a porous medium, the nonlinear inertial effects Whitaker (1996) are negligible and the governing equations reduce to either the Darcy-Brinkman equation or Darcy's law when the Laplacian term can be neglected; see Appendix B. For their theoretical derivation, we refer for example to

Whitaker's works Whitaker (1969, 1986); Barrère et al. (1992); Whitaker (1999) with the volume averaging method. The two-scale homogenization method states similar upscaling equations, e.g. Sanchez-Palencia (1980, 1983); Hornung (1997). Then, the coupling of macroscale models in fluid-porous systems considers the Stokes/Darcy-Brinkman problem below:

$$\begin{cases} \boldsymbol{\nabla}\cdot\mathbf{v} = 0 & \text{in } \Omega_f \cup \Omega_p, \\ -\mu\,\Delta\mathbf{v} + \nabla p = \rho\,\boldsymbol{f} & \text{in } \Omega_f, \\ -\dfrac{\mu}{\phi_p}\,\Delta\mathbf{v} + \mu\,\boldsymbol{K}_p^{-1}\cdot\mathbf{v} + \nabla p = \rho\,\boldsymbol{f} & \text{in } \Omega_p, \end{cases} \tag{3}$$

where μ is the dynamic viscosity of the fluid, ρ its mass density, ϕ_p the porosity (volume fraction of fluid pores), $\boldsymbol{K}_p$ the intrinsic permeability tensor of the porous region Ω_p, $\mathbf{v}$ denotes the filtration velocity defined as the superficial average and p the pressure as an intrinsic average. The external force per mass unit $\boldsymbol{f}$, e.g. gravity acceleration $\boldsymbol{f} = \boldsymbol{g}$, is included in the right-hand side. The Darcy number Da is classically introduced as a dimensionless parameter to characterize the flow in the porous medium, see Appendix A:

$$\mathrm{Da} := \frac{K_p}{L^2}, \tag{4}$$

where $K_p := \|\boldsymbol{K}_p\|$ is a suitable matrix norm (or semi-norm) of the tensor $\boldsymbol{K}_p$. A practical criterion based on the (dimensionless) Brinkman number Br[3]:

$$\mathrm{Br} := \frac{K_p(\phi_p)}{L^2\,\phi_p} = \frac{\mathrm{Da}(\phi_p)}{\phi_p}, \tag{5}$$

is proposed in Appendix B to determine whether or not the Brinkman viscous term can be neglected with respect to Darcy's drag. Then it appears in figure 24 that it is fully justified, *i.e.* $\mathrm{Br} \ll 1$, within the porosity range $0 < \phi_p \leq 0.95$ when the macroscale length L satisfies $L \gtrsim 20\,\ell$ (ℓ being the size of the representative unit cell in the porous medium in figure 1). In that conditions, the fluid-porous coupling reduces to the following Stokes/Darcy problem that is mainly studied in the literature:

$$\begin{cases} \boldsymbol{\nabla}\cdot\mathbf{v} = 0 & \text{in } \Omega_f \cup \Omega_p, \\ -\mu\,\Delta\mathbf{v} + \nabla p = \rho\,\boldsymbol{f} & \text{in } \Omega_f, \\ \mu\,\boldsymbol{K}_p^{-1}\cdot\mathbf{v} + \nabla p = \rho\,\boldsymbol{f} & \text{in } \Omega_p. \end{cases} \tag{6}$$

The macroscale problems (3) and (6) must be closed by adding physically relevant, reliable and calibrated interface conditions on a dividing surface Σ, and suitable boundary conditions as well, to provide well-posed and globally dissipative coupled problems ready to use for the simulations of applications. The sets of interface conditions should cover the whole porosity range $0 < \phi_p < 1$, be valid for arbitrary flow directions and take account of anisotropic effects. Using asymptotic analysis of the

[3] Up to the authors' knowledge, it seems to be the first time that this number is introduced in the literature, although Brinkman's screening length is used.

thin transition region Ω_{fp} of thickness d, a family of jump interface conditions at the first order $O(d/L)$ and parametrized by the position $\xi := |z_\Sigma|/d$ with $0 \le \xi \le 1$ of the dividing surface Σ inside Ω_{fp} are derived theoretically in Angot et al. (2017). These interface conditions are summarized in the next section after the introduction of some notations.

2.1 The general asymptotic interface model of *Angot et al. (2017)*

Let $\boldsymbol{n}$ be a unit normal vector on the dividing surface Σ arbitrarily directed from Ω_p to Ω_f and $\boldsymbol{\tau}$ be any unit tangential vector on Σ; see figures 2 and 3. The couple of vectors $(\boldsymbol{\tau}_1, \boldsymbol{\tau}_2)$ denotes a local orthonormal basis of tangential vectors on the surface Σ, the unit vector $\boldsymbol{\tau}$ being any of these vectors. For any quantity ψ defined all over Ω, the restrictions on Ω_f or Ω_p are respectively denoted by $\psi^f := \psi_{|\Omega_f}$ and $\psi^p := \psi_{|\Omega_p}$. For a function ψ having a jump on Σ, let ψ^- and ψ^+ be the traces of ψ^p and ψ^f on each side of Σ, respectively. Following (Angot 2010, 2011), the jump of ψ on Σ oriented by $\boldsymbol{n}$ and the arithmetic mean of traces of ψ are defined as reduced variables at the interface by:

$$\begin{cases} [\![\psi]\!]_\Sigma := \psi^+ - \psi^- = \left(\psi^f - \psi^p\right)_\Sigma, \\ \overline{\psi}_\Sigma := \dfrac{1}{2}\left(\psi^+ + \psi^-\right) = \dfrac{1}{2}\left(\psi^f + \psi^p\right)_\Sigma. \end{cases} \tag{7}$$

We also define the weighted mean $\overline{\psi}^w_\Sigma$ for using a non-centered approximation at a dividing surface $\Sigma = \Sigma_\xi$ located at $z_\Sigma := -d + (1-\xi)\,d$ in Ω_{fp} with $\xi := |z_\Sigma|/d$ and $0 \le \xi = |z_\Sigma|/d \le 1$:

$$\overline{\psi}^w_\Sigma := \overline{\psi}_\Sigma + \left(\frac{1}{2} - \xi\right)[\![\psi]\!]_\Sigma = \begin{cases} \psi^f_\Sigma & \text{if } \xi = 0 \quad \text{i.e.} \quad \Sigma = \Sigma_t \text{ at } z = 0 \\ \overline{\psi}_\Sigma & \text{if } \xi = 1/2 \quad \text{i.e.} \quad \Sigma = \Sigma_m \text{ at } z = -d/2 \\ \psi^p_\Sigma & \text{if } \xi = 1 \quad \text{i.e.} \quad \Sigma = \Sigma_b \text{ at } z = -d. \end{cases} \tag{8}$$

Besides, for any quantity k, the arithmetic and harmonic means over the thickness d of Ω_{fp} are respectively given by:

$$\langle k \rangle(x) := \frac{1}{d}\int_{-d/2}^{d/2} k(x,z)\,\mathrm{d}z, \qquad \text{and} \qquad \langle k \rangle^h(x) := \left\langle \frac{1}{k} \right\rangle^{-1}. \tag{9}$$

The general asymptotic interface model supplies a set of jump interface conditions for the stress and tangential velocity vectors at a sharp dividing surface Σ inside Ω_{fp}. They are valid to couple both the Stokes/Darcy-Brinkman or the Stokes/Darcy models, just by changing the definition of the stress vector. For a Newtonian fluid, the Cauchy stress vector $\boldsymbol{\sigma}(\mathbf{v}, p)\cdot\boldsymbol{n}$ on Σ is defined by:

$$\begin{cases} \boldsymbol{\sigma}(\mathbf{v}, p)\cdot\boldsymbol{n} := \boldsymbol{\sigma}_v(\mathbf{v})\cdot\boldsymbol{n} - p\,\boldsymbol{n} & \text{where:} \\ \boldsymbol{\sigma}_v(\mathbf{v})\cdot\boldsymbol{n} := \widetilde{\mu}\left(\nabla\mathbf{v} + \nabla\mathbf{v}^T\right)\cdot\boldsymbol{n} & \text{with} \quad \widetilde{\mu} := \dfrac{\mu}{\phi}, \\ & \text{and} \quad \phi = 1 \text{ in } \Omega_f, \quad \phi = \phi_p \text{ in } \Omega_p, \end{cases} \tag{10}$$

where $\boldsymbol{\sigma}_v(\mathbf{v})\cdot\boldsymbol{n}$ denotes the viscous stress vector and $\widetilde{\mu}=\mu/\phi$ is the effective viscosity in the porous medium from (Whitaker 1999, Chapter 4) or (Valdés-Parada et al. 2007b). Thus, the latter definition holds for the Stokes and Darcy-Brinkman equations but with the Darcy equation in Ω_p, the stress vector reduces to the normal pressure force with no viscous stress:

$$\boldsymbol{\sigma}^p(\mathbf{v},p)\cdot\boldsymbol{n} := -p^p\,\boldsymbol{n} \quad \text{ in } \Omega_p. \tag{11}$$

Then, the general asymptotic interface model on Σ for the non-inertial regime and arbitrary flow directions reads up to $O(d/L)$ with a surface force $\boldsymbol{f}_\Sigma := d\,\langle\rho\boldsymbol{f}\rangle$:

$$\begin{cases} [\![\mathbf{v}\cdot\boldsymbol{n}]\!]_\Sigma = 0, \\ \overline{\boldsymbol{\sigma}_v(\mathbf{v})\cdot\boldsymbol{n}_\Sigma}^{\,w} = \dfrac{\mu}{\sqrt{K_p}}\,\alpha_\Sigma\,[\![\mathbf{v}]\!]_\Sigma, \\ [\![\boldsymbol{\sigma}(\mathbf{v},p)\cdot\boldsymbol{n}]\!]_\Sigma = \dfrac{\mu}{\sqrt{K_p}}\,\boldsymbol{\beta}_\Sigma\cdot\bar{\mathbf{v}}_\Sigma^{\,w} + \boldsymbol{f}_\Sigma \end{cases} \quad \text{on } \Sigma. \tag{12}$$

The dimensionless velocity slip scalar coefficient α_Σ and friction tensor $\boldsymbol{\beta}_\Sigma$ of stress jump at the interface included in (12) are defined as below:

$$\begin{cases} \alpha_\Sigma := \dfrac{\sqrt{K_p}}{d\,\phi_\Sigma} & \text{with} \quad \phi_\Sigma := \dfrac{1}{\langle\phi^{-1}\rangle} \\ \boldsymbol{\beta}_\Sigma := d\,\sqrt{K_p}\,\boldsymbol{K}_\Sigma^{-1} & \text{with} \quad \boldsymbol{K}_\Sigma^{-1} := \langle\boldsymbol{K}^{-1}(\phi)\rangle, \end{cases} \tag{13}$$

where ϕ_Σ denotes an effective surface porosity on Σ and $\boldsymbol{K}_\Sigma$ is an effective surface permeability tensor on Σ. Coming from the symmetric permeability tensor $\boldsymbol{K}$ in Ω_{fp}, the friction tensor $\boldsymbol{\beta}_\Sigma$ defined in (13) can be expected to remain symmetric too within the calibration procedure.

Remark 1 (Contribution of $\nabla\mathbf{v}^T$ in the slip coefficient α_Σ.) The derivation in Angot et al. (2017) is carried out using the pseudo-stress vector: $\widetilde{\mu}\nabla\mathbf{v}\cdot\boldsymbol{n}-p\,\boldsymbol{n}$ in Ω_{fp} instead of the full stress one $\boldsymbol{\sigma}(\mathbf{v},p)\cdot\boldsymbol{n}$ given by (10) that is more suitable for arbitrary flow directions Jones (1973). Indeed, the contribution of $\nabla\mathbf{v}^T$ in the averaging of the full stress vector over Ω_{fp} is negligible because it is shown in (Angot et al. 2017, Section III.B.2) that all the terms with tangential derivatives can be neglected up to $O(d/L)$ and because we have also $[\![\mathbf{v}\cdot\boldsymbol{n}]\!]_\Sigma = 0$ with (12). This observation is also pointed out in (Angot et al. 2021, Footnote #4).

Remark 2 (Taking account of additional jumps in the coefficients α_Σ or $\boldsymbol{\beta}_\Sigma$.) Let us notice that the coefficients in (13), being defined by integrals over Ω_{fp}, do not depend on the position ξ of the dividing surface Σ_ξ inside Ω_{fp}. Therefore, the asymptotic modelling theory cannot predict the dependence of α_Σ or $\boldsymbol{\beta}_\Sigma$ with respect to the location of the dividing surface Σ_ξ inside Ω_{fp}, but the theory does predict the related explicit expressions (12) of the jump conditions on Σ_ξ. Moreover, it is important to recall that the starting point of the asymptotic theory developed in Angot et al. (2017) by averaging the one-domain mass and momentum transport equations over Ω_{fp} assumes continuity of both the velocity and stress vectors at the upper and lower

boundaries of Ω_{fp}. This does not require that the porosity transition function ϕ or the permeability $\boldsymbol{K}(\phi)$ in Ω_{fp} should be continuous inside or at the latter boundaries varying from $\phi_f = 1$ to ϕ_p; see the proof in Angot (1999). In particular, Heaviside steps are admitted as in the approach of Neale and Nader (1974); Angot (1999), but obviously, more accurate results can be expected from the one-domain solution of the full General Transport Equations in Brinkman's viscous boundary layer; see Hernandez-Rodriguez et al. (2020, 2022). Therefore, jumps of velocity or stress existing before the averaging over Ω_{fp} must be taken into account by modifying the values of α_Σ or $\boldsymbol{\beta}_\Sigma$ given in (13), respectively. This is the case when the two-domain model considers the coupling of the Stokes/Darcy problem that introduces an additional stress jump by neglecting the viscous stress vector in the Darcy/Brinkman model replaced by Darcy's law in Ω_p. Therefore, the value of $\boldsymbol{\beta}_\Sigma$ should be obviously modified consistently.

For example in the isotropic case, (13) gives analytic expressions of the scalar slip and friction coefficients at the interface as functions of porosity ϕ_p. As made in Angot et al. (2021), these coefficients can be estimated using the two-point trapezoidal rule to evaluate the integrals over Ω_{fp} since only the known values in Ω_f and Ω_p are involved with $\phi_f = 1$ and ϕ_p, respectively. In this case, we get with the trapezoidal quadrature:

$$\begin{cases} \alpha_\Sigma(\phi_p) \simeq \dfrac{\sqrt{K_p(\phi_p)}}{2\,d(\phi_p)}\left(1+\dfrac{1}{\phi_p}\right), \\ \beta_\Sigma(\phi_p) \simeq \dfrac{d(\phi_p)}{2\sqrt{K_p(\phi_p)}}\,. \end{cases} \tag{14}$$

It is interesting to express the relations (14) with the dimensionless quantities of the problem: the Darcy number $\mathrm{Da}(\phi_p) := K_p(\phi_p)/L^2$ and the dimensionless thickness of the transition layer $\delta(\phi_p) := d(\phi_p)/L$. That gives:

$$\begin{cases} \alpha_\Sigma(\phi_p) \simeq \dfrac{\sqrt{\mathrm{Da}(\phi_p)}}{2\,\delta(\phi_p)}\left(1+\dfrac{1}{\phi_p}\right), \\ \beta_\Sigma(\phi_p) \simeq \dfrac{\delta(\phi_p)}{2\sqrt{\mathrm{Da}(\phi_p)}}\,. \end{cases} \tag{15}$$

Although the variation profiles of porosity and permeability are not known *a priori* for the microstructure in the inter-region, the three-point Simpson quadrature formula with the mid-point of porosity $(1+\phi_p)/2$ is likely to provide a more accurate approximation. Indeed, as shown in figure 4, the reasonable porosity transition functions in Ω_{fp} for the single-domain continuum modelling pass through this mid-point.

The case where the dividing surface Σ is chosen in the middle of the transition layer, *i.e.* $\Sigma = \Sigma_m$ with $\xi = 1/2$ is mainly discussed in Angot et al. (2017). Moreover, both the unsteady Stokes/Darcy-Brinkman and Stokes/Darcy coupled problems supplemented by the set of jump interface conditions (12) on $\Sigma = \Sigma_m$ with $\xi = 1/2$ are proved to be globally well-posed in time, whatever the size of the data, in Angot (2018). The proof for the corresponding steady cases was carried out in Angot (2011). Therefore in the present study, we focus on and discuss the two other special cases where either $\Sigma = \Sigma_t$

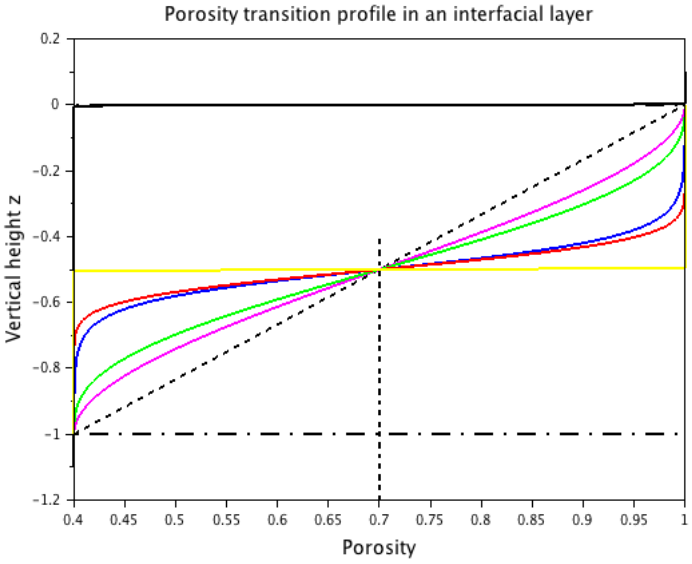

Fig. 4 Porosity transition profiles in an interfacial region Ω_{fp} for the single-domain continuum modelling with $\phi_p = 0.40$, $d = \ell$ and different functions: ramp (black dotted), third-order polynomial (magenta), fifth-order polynomial (green), sigmoid (blue), Gauss error (red), Heaviside step at top surface (black solid line), Heaviside step at middle surface (yellow).

with $\xi = 0$ or $\Sigma = \Sigma_b$ with $\xi = 1$. We show further that the simplifications induced by the weighted mean (8) reported in (12) supplies more practical jump interface conditions and a set of optimal ones minimizing the loss of flow rate for both the Stokes/Darcy-Brinkman and Stokes/Darcy problems.

2.2 Jump interface condition on Σ_t at $z = 0$ with $\xi = 0$

When the dividing surface Σ is chosen at the top of the inter-region, *i.e.* $\Sigma = \Sigma_t$ with $\xi = 0$ as shown in figure 2, then the set of jump interface conditions (12, 8) reduces to:

$$\begin{cases} [\![\mathbf{v}\cdot\boldsymbol{n}]\!]_\Sigma = 0, \\ \boldsymbol{\sigma}_v^f(\mathbf{v})\cdot\boldsymbol{n}_\Sigma = \dfrac{\mu}{\sqrt{K_p}}\,\alpha_\Sigma\,[\![\mathbf{v}]\!]_\Sigma, \\ [\![\boldsymbol{\sigma}(\mathbf{v},p)\cdot\boldsymbol{n}]\!]_\Sigma = \dfrac{\mu}{\sqrt{K_p}}\,\boldsymbol{\beta}_\Sigma\cdot\mathbf{v}_\Sigma^f + \boldsymbol{f}_\Sigma \end{cases} \quad \text{on } \Sigma = \Sigma_t. \tag{16}$$

Compared to (2), the present set of interface conditions (16) gives a theoretical justification to a far more general form than the *ad-hoc* extended Beavers-Joseph conditions (2) assumed up to now in the literature for coupling the multi-dimensional Stokes/Darcy problem with a velocity slip conditions at Σ_t. Indeed, an additional stress

jump on Σ_t is required. So, it is fully original up to our knowledge since it appears as a proper generalization for the multi-dimensional flow of the conditions including jumps of both tangential velocity and shear stress derived by several methods for the 1-D channel flow in Cieszko and Kubik (1999); Kubik and Cieszko (2005); Valdés-Parada et al. (2013). Firstly, the set (16) is directly derived in the case of multi-dimensional flows and it is thus valid for arbitrary flow directions. Moreover, by including the tensorial quantity $\boldsymbol{\beta}_\Sigma$, the set (16) is inherently well-suited to take into account the anisotropic effects on the flow due to the microstructure.

Coupling the multi-dimensional Stokes/Darcy-Brinkman problem with the stress jump condition (19) is also completely new in the literature, and it appears as a nice generalization for the multi-dimensional flow of the condition of Ochoa-Tapia and Whitaker (1995a,b), also studied in Goyeau et al. (2003); Valdés-Parada et al. (2009a). Indeed, the latter condition was derived for the 1-D channel flow parallel to the porous bed by assuming the tangential velocity continuity $[\![\mathbf{v}\cdot\boldsymbol{\tau}]\!]_\Sigma = 0$ on Σ_t at $z = 0$. However until now, there was no evidence that such an hypothesis holds. That is the reason why it is derived by Valdés-Parada et al. (2013), for the same flow configuration, a generalization including also a jump of tangential velocity at some unknown dividing surface inside the interfacial region Ω_{fp}. In fact, we show in the next Section 4 that the latter assumption $[\![\mathbf{v}\cdot\boldsymbol{\tau}]\!]_\Sigma = 0$ on Σ_t at $z = 0$ is not valid unless to consider negative values of the shear-stress jump $\beta_\Sigma < 0$ on Σ_t that appears to be unreasonable for the energy dissipation; see Section 3. Let us also mention that an interface condition of the type (16) is also predicted in Section 4 for the coupling of the Stokes/Darcy-Brinkman problem with no shear-stress jump, thus having only a normal stress jump and a velocity slip on $\Sigma = \Sigma_t$. Then, it yields with $\boldsymbol{f} = 0$:

$$\begin{cases} [\![\mathbf{v}\cdot\boldsymbol{n}]\!]_\Sigma = 0, \\ \boldsymbol{\sigma}_v^f(\mathbf{v})\cdot\boldsymbol{n}_\Sigma = \dfrac{\mu}{\sqrt{K_p}}\,\alpha_\Sigma\,[\![\mathbf{v}]\!]_\Sigma, \\ [\![\boldsymbol{\sigma}(\mathbf{v},p)\cdot\boldsymbol{n}]\!]_\Sigma = \dfrac{\mu}{\sqrt{K_p}}\,\boldsymbol{\beta}_\Sigma\cdot\mathbf{v}_\Sigma^f \qquad \text{with } \beta_\tau = 0 \end{cases} \qquad \text{on } \Sigma = \Sigma_t, \tag{17}$$

where the first diagonal coefficients of $\boldsymbol{\beta}_\Sigma$ vanishes, *i.e.* $\beta_\tau = 0$. This is also a quite unsual approach to deal with the Stokes/Darcy-Brinkman problem that classically uses a shear-stress jump condition as derived for the 1-D channel flow in Ochoa-Tapia and Whitaker (1995a); Valdés-Parada et al. (2013). However for the Stokes/Darcy coupling, even for the 1-D pressure-driven channel flow with any isotropic microstructure, an interface condition having only a velocity slip with no shear-stress jump seems impossible to reach and unrealistic. This confirms the foregoing discussion about the set (2).

2.3 Jump interface condition on Σ_b at $z = -d$ with $\xi = 1$

When the dividing surface Σ is chosen at the bottom of the inter-region, *i.e.* $\Sigma = \Sigma_b$ with $\xi = 1$ as shown in figure 3, then the set of jump interface conditions (12, 8)

reduces to:

$$\begin{cases} [\![\mathbf{v}\cdot\boldsymbol{n}]\!]_\Sigma = 0, \\ \boldsymbol{\sigma}_v^p(\mathbf{v})\cdot\boldsymbol{n}_\Sigma = \dfrac{\mu}{\sqrt{K_p}}\alpha_\Sigma\,[\![\mathbf{v}]\!]_\Sigma, \\ [\![\boldsymbol{\sigma}(\mathbf{v},p)\cdot\boldsymbol{n}]\!]_\Sigma = \dfrac{\mu}{\sqrt{K_p}}\boldsymbol{\beta}_\Sigma\cdot\mathbf{v}_\Sigma^p + \boldsymbol{f}_\Sigma \end{cases} \quad \text{on } \Sigma = \Sigma_b. \tag{18}$$

Using such a condition (18) on Σ_b means in practice that the pure fluid region is extended downwards at the macroscale to include the whole transition layer. In other words, the two-domain model replaces in that case the interfacial layer Ω_{fp} of the one-domain model by a free fluid region. As for (16), the set (18) is well-adapted for arbitrary flow directions and for capturing the anisotropic effects of the microstructure on the flow by calibrating the friction tensor $\boldsymbol{\beta}_\Sigma$.

Moreover, an important simplification of (18) occurs when it is used for the coupling of the Stokes/Darcy problem. Indeed, the viscous stress vector for Darcy's law being zero, *i.e.* $\boldsymbol{\sigma}_v^p(\mathbf{v})\cdot\boldsymbol{n}_\Sigma = 0$, then since $\alpha_\Sigma > 0$, we get: $[\![\mathbf{v}]\!]_\Sigma = 0$. Therefore, this yields the following stress jump interface condition with continuous velocity $\mathbf{v}_\Sigma^f = \mathbf{v}_\Sigma^p = \mathbf{v}_\Sigma$ on Σ_b for the Stokes/Darcy problem:

$$\begin{cases} [\![\mathbf{v}]\!]_\Sigma = 0, \\ [\![\boldsymbol{\sigma}(\mathbf{v},p)\cdot\boldsymbol{n}]\!]_\Sigma = \dfrac{\mu}{\sqrt{K_p}}\boldsymbol{\beta}_\Sigma\cdot\mathbf{v}_\Sigma + \boldsymbol{f}_\Sigma \end{cases} \quad \text{on } \Sigma = \Sigma_b. \tag{19}$$

This set of interface conditions is not found in the literature and completely in rupture with usual Beavers-Joseph's concept of velocity slip for the Stokes/Darcy problem or with its numerous extensions up to now.

Furthermore, we show in the next Section 4 that the set (19) also holds for the coupling of the Stokes/Darcy-Brinkman problem. Indeed at least for the one-dimensional flow, there exists a unique optimal interface Σ_b that can be determined, where the continuity of velocity is satisfied and such that the stress jump condition (19) minimizes the loss of volumic flow rate while keeping $\boldsymbol{\beta}_\Sigma \geq 0$, *i.e.* as a semi-definite positive matrix to ensure the global dissipation; see Section 3. The generalization of this result for multi-dimensional flows seems surely valid as well by manipulating geometry and intersection of surfaces.

Finally, it is important to emphasize that omong all the sets of conditions (16, 17, 18) and (19) investigated in Section 4, only the set (19) provides the optimal interface conditions that minimize the loss of flow rate while satisfying the energy dissipation whatever the coupling problem, Stokes/Darcy-Brinkman or Stokes/Darcy, and for any pressure-driven or shear-driven flow benchmark. Moreover, the inherent tensorial form of all the latter interface conditions ensures that it should be possible to handle flows over isotropic, orthotropic and fully anisotropic porous media.

2.4 Comparison with the volume averaging method for the one-dimensional flow

In this section, the jump boundary conditions derived using the asymptotic model are compared to those established with the volume averaging method (VAM) (Valdés-Parada et al. 2013). This comparison is performed by considering the one-dimensional parallel flow. Let us recall that the jump conditions derived with VAM take the form:

$$\frac{\partial(\mathbf{v}^f\cdot\boldsymbol{\tau})}{\partial n}_{|\Sigma} - \alpha_{fp}\frac{\alpha}{\sqrt{K_p}}\frac{\partial(\mathbf{v}^p\cdot\boldsymbol{\tau})}{\partial n}_{|\Sigma} = \frac{\alpha}{\sqrt{K_p}}\left(\mathbf{v}^f - \phi_p\theta\mathbf{v}^p\right)_{|\Sigma}\cdot\boldsymbol{\tau} \tag{20}$$

$$\frac{\partial(\mathbf{v}^p\cdot\boldsymbol{\tau})}{\partial n}_{|\Sigma} - \omega\frac{\partial\mathbf{v}^f\cdot\boldsymbol{\tau})}{\partial n}_{|\Sigma} = \frac{\phi_p\beta}{\sqrt{K_p}}\left(\mathbf{v}^p - \beta_{fp}\mathbf{v}^f\right)_{|\Sigma}\cdot\boldsymbol{\tau} \tag{21}$$

where the six coefficients α_{fp}, α, θ, ω, β and β_{fp} are dependent on the local microstructure of the inter-region and the location of the dividing surface. Note that to easily compare the calibration results with usual configurations in the literature, the upper surface of transition layer is now located at $z = 0$ and thus the lower surface is at $z = -d$. Therefore, for the one-dimensional parallel flow, the velocity and the stress jump conditions in (12) take respectively the form

$$\frac{\partial(\mathbf{v}^f\cdot\boldsymbol{\tau})}{\partial n}_{|\Sigma} - \frac{\xi}{(1-\xi)}\frac{\partial(\mathbf{v}^p\cdot\boldsymbol{\tau})}{\partial n}_{|\Sigma} = \frac{1}{\phi_\Sigma\, d(1-\xi)}\left(\mathbf{v}^f - \mathbf{v}^p\right)\cdot\boldsymbol{\tau} \tag{22}$$

$$\frac{\partial(\mathbf{v}^p\cdot\boldsymbol{\tau})}{\partial n}_{|\Sigma} - \phi_p\frac{\partial(\mathbf{v}^f\cdot\boldsymbol{\tau})}{\partial n}_{|\Sigma} = \frac{\phi_p\, d\,\xi}{< K(\phi,\nabla\phi) >^h}\left(\mathbf{v}^p - \frac{(1-\xi)}{\xi}\mathbf{v}^f\right)\cdot\boldsymbol{\tau} \tag{23}$$

The comparison between (22) and (20) gives

$$\begin{cases} \theta = \dfrac{1}{\phi_p} \\ \alpha_\Sigma = \dfrac{\sqrt{K_p}}{d\phi_\Sigma(1-\xi)} = \dfrac{\sqrt{K_p}(1+\phi_p)}{2d\phi_p(1-\xi)} \\ \eta_{fp} = \dfrac{\phi_\Sigma d\xi}{\phi^p} = 2d\xi(1+\phi_p) \end{cases} \tag{24}$$

Similarly, the comparison between (23) and (21) leads to

$$\begin{cases} \omega = \phi_p \\ \beta_{fp} = \dfrac{(1-\xi)}{\xi} \\ \beta_\Sigma = \dfrac{d\,\xi\sqrt{K_p}}{< K(\phi,\nabla\phi) >^h} = \dfrac{d\,\xi}{2\sqrt{K_p}} \end{cases} \tag{25}$$

The jump coefficients α_Σ and β_Σ in (24) and (25), respectively, are similar to the expressions provided in (14) and (15), the difference being the dependence on the location of the dividing surface ξ ($0 \le \xi \le 1$). This illustrates that the volume averaging method and the asymptotic method lead to the same interfacial modelling.

As done in sections 2.2 and 2.3, let us examine the two limiting locations of the dividing surface. First, we consider the location in Σ_t where $\xi = 0$. therefore, (22) and (23) take the form

$$\frac{\partial(\mathbf{v}^f \cdot \boldsymbol{\tau})}{\partial n_{|\Sigma}} = \frac{1}{\phi_\Sigma\, d}\left(\mathbf{v}^f - \mathbf{v}^p\right) \cdot \boldsymbol{\tau} = \frac{\alpha_{bj}}{\sqrt{K_p}}\left(\mathbf{v}^f - \mathbf{v}^p\right) \cdot \boldsymbol{\tau} \tag{26}$$

$$\phi_p \frac{\partial(\mathbf{v}^f \cdot \boldsymbol{\tau})}{\partial n}_{|\Sigma} - \frac{\partial(\mathbf{v}^p \cdot \boldsymbol{\tau})}{\partial n}_{|\Sigma} = \frac{\phi_p\, d}{< K(\phi, \nabla\phi) >^h} \mathbf{v}^f \cdot \boldsymbol{\tau} \tag{27}$$

where (26) represents the slip condition introduced by Beavers and Joseph (1967). The dimensionless slip coefficient is deduced from (26) to give

$$\alpha_{bj} = \frac{\sqrt{K_p}}{\phi_\Sigma\, d} \tag{28}$$

Since this analysis is based on the Stokes/Darcy-Brinkman model, and in accordance with (16), the second interfacial equation (27) represents the shear stress jump condition.
Keeping $\xi = 0$, let us now consider the Stokes/Darcy model instead of the Stokes/Darcy-Brinkman one. In that case, (26) remains unchanged while (27) reduces to

$$\frac{\partial(\mathbf{v}^f \cdot \boldsymbol{\tau})}{\partial n}_{|\Sigma} = \frac{d}{< K(\phi, \nabla\phi) >^h} \mathbf{v}^f \cdot \boldsymbol{\tau} \tag{29}$$

Equation (29) is in fact the Safman's form of the Beavers and Joseph condition where the velocity in the porous region $\mathbf{v}^p$ can be neglected since it is small compared to the velocity in the fluid channel $\mathbf{v}^f$. Using the same simplification in (26), leads to the compatibility condition

$$\frac{d}{< K(\phi, \nabla\phi) >^h} = \frac{1}{\phi_\Sigma\, d} \tag{30}$$

giving rise to the following expression for the thickness of the transition layer

$$d = \sqrt{\frac{2K_p}{\phi_\Sigma}} \tag{31}$$

Expression (31) is in good agreement with the scaling obtained in Angot et al. (2017). Therefore, it is easy to show that

$$\alpha_{bj} = \sqrt{\frac{2}{\phi_\Sigma}} \tag{32}$$

and due to the expression for ϕ_Σ in (13),

$$\alpha_{bj} = \sqrt{\frac{1+\phi_p}{\phi_p}} \tag{33}$$

Finally, if we now consider the case where the dividing surface is located at Σ_b where $\xi = 1$ (see section 2.3). In that case, the jump conditions (24) and (25) become:

$$\frac{\partial(\mathbf{v}^p \cdot \boldsymbol{\tau})}{\partial n}_{|\Sigma} = \frac{1}{\phi_\Sigma d}\left(\mathbf{v}^f - \mathbf{v}^p\right) \cdot \boldsymbol{\tau}, \tag{34}$$

$$\frac{\partial(\mathbf{v}^p \cdot \boldsymbol{\tau})}{\partial n}_{|\Sigma} - \phi^p \frac{\partial(\mathbf{v}^f \cdot \boldsymbol{\tau})}{\partial n}_{|\Sigma} = \frac{\phi^p d}{< K(\phi, \nabla\phi) >^h} \mathbf{v}^p \cdot \boldsymbol{\tau}. \tag{35}$$

Unlike to Ochoa-Tapia and Whitaker (1995), the Stokes/Darcy-Brinkman model gives two jump boundary conditions when the dividing surface is at Σ_b which is in agreement with the conclusion of Valdés-Parada et al. (2013). Moreover, if we assume like in Ochoa-Tapia and Whitaker (1995) the continuity of velocity, then the stress jump condition (35) becomes:

$$\frac{\partial(\mathbf{v}^f \cdot \boldsymbol{\tau})}{\partial n}_{|\Sigma} = \frac{d}{< K(\phi, \nabla\phi) >^h} \mathbf{v}^f \cdot \boldsymbol{\tau}. \tag{36}$$

Therefore, the comparison of (36) with the shear stress condition of Ochoa-Tapia and Whitaker (1995a) for the Stokes/Darcy-Brinkman model gives the stress jump coefficient:

$$\beta_{otw} = \frac{\mathrm{d}}{2\sqrt{K_p}}. \tag{37}$$

Finally, if the Stokes/Darcy model is considered as made in section (2.3), the jump of tangential velocity is zero and therefore we get continuity of velocity at Σ_b and the stress jump condition (36) is still valid.

In conclusion, this comparison shows that the volume averaging method and the asymptotic method lead to the same interfacial momentum modelling for the one-dimensional flow. From the general point of view, this analysis based on the Stokes/Darcy-Brinkman model confirms that both velocity and stress jump conditions must be imposed at a dividing surface whose location strongly impacts their forms. For the Stokes/Darcy model, the velocity slip condition proposed by Beavers and Joseph is recovered at Σ_t. On the other hand, assuming continuity of velocity gives the stress jump condition derived by Ochoa-Tapia and Whitaker for the Stokes/Darcy-Brinkman model.

3 The mechanical energy balance and global dissipation

The dissipation of mechanical energy inside the whole fluid-porous system is an important issue that is very rarely tackled in the literature. Here, the energy balance of the resulting macroscale coupled models (3) or (6) in the domain $\Omega := \Omega_f \cup \Sigma \cup \Omega_p$, *i.e.* the Stokes and Darcy-Brinkman or Darcy equations in Ω_f and Ω_p, respectively, supplemented by the interface conditions (16) on Σ_t (figure 2) or (19) on Σ_b (figure 3). This will show that these coupled models actually satisfy the energy theorem in mechanics at the macroscopic scale and that the conservation of energy holds.

Without loss of generality, we assume null boundary conditions $\mathbf{v}^f_{|\Gamma} = 0$ and $\mathbf{v}^p_{|\Gamma} = 0$ (for the Darcy-Brinkman law in (3) in Ω_p) or $\mathbf{v}^p \cdot \boldsymbol{n}_{|\Gamma} = 0$ (for the Darcy law in (6) in

Ω_p) at the external boundary Γ of Ω. The motion governing equations (3) or (6) can be written in the conservative form using the Cauchy stress tensor defined in (10) or (11). Then, with μ and ϕ_p being constant, we use the fact that: $\boldsymbol{\nabla}\cdot(\nabla\mathbf{v}^T)=0$ since $\boldsymbol{\nabla}\cdot\mathbf{v}=0$. By taking the L^2-scalar products with $\mathbf{v}$ of the motion equations in (3) in Ω_f and Ω_p, respectively, we use formally standard integrations by parts for sufficiently regular solutions to give a sense to the integrals over the interface Σ. So, all the boundary integrals on Γ will vanish with the homogeneous boundary conditions, as well as the integrals with divergence-free velocity terms. The interface conditions are incorporated as in Angot (2010, 2011) in the integrals over Σ, the rigourous analysis being carried out in Angot (2018). Then, it yields the following mechanical energy balance:

$$\begin{aligned}\int_{\Omega_f}\mu\,|\nabla\mathbf{v}^f|^2\,\mathrm{d}x+\int_{\Omega_p}\frac{\mu}{\phi_p}\,|\nabla\mathbf{v}^p|^2\,\mathrm{d}x+\int_{\Omega_p}\mu\,(\boldsymbol{K}_p^{-1}\cdot\mathbf{v}^p)\cdot\mathbf{v}^p\,\mathrm{d}x\\ +I_\Sigma=\int_\Omega\rho\boldsymbol{f}\cdot\mathbf{v}\,\mathrm{d}x-\int_\Sigma\boldsymbol{f}_\Sigma\cdot\overline{\mathbf{v}}_\Sigma\,\mathrm{d}s,\end{aligned}\tag{38}$$

where the energy quantity I_Σ gathers all the contributions of the interface conditions, either (16) on Σ_t or (19) on Σ_b. Following (Angot 2010, Eqs. (10,11)) or Angot (2011), the interface term I_Σ reads:

$$\begin{aligned}I_\Sigma&=\int_\Sigma\Big(\boldsymbol{\sigma}^f(\mathbf{v},p)\cdot\boldsymbol{n}\Big)\cdot\mathbf{v}^f\,\mathrm{d}s-\int_\Sigma(\boldsymbol{\sigma}^p(\mathbf{v},p)\cdot\boldsymbol{n})\cdot\mathbf{v}^p\,\mathrm{d}s\\&=\int_\Sigma\overline{\boldsymbol{\sigma}(\mathbf{v},p)\cdot\boldsymbol{n}}_\Sigma\cdot[\![\mathbf{v}]\!]_\Sigma\,\mathrm{d}s+\int_\Sigma[\![\boldsymbol{\sigma}(\mathbf{v},p)\cdot\boldsymbol{n}]\!]_\Sigma\cdot\overline{\mathbf{v}}_\Sigma\,\mathrm{d}s.\end{aligned}\tag{39}$$

The right-hand side in Eq. (38) is equal to the total work of all external forces in the fluid-porous system. Moreover, the second term in the left-hand side of (38) must be discarded when the Stokes/Darcy model (6) is considered since the viscous stress is then neglected in the porous medium Ω_p.

3.1 Energy balance for the fluid-porous flow with interface conditions (16) on Σ_t

Using the definitions (7), we have:

$$\overline{\boldsymbol{\sigma}(\mathbf{v},p)\cdot\boldsymbol{n}}_\Sigma=\boldsymbol{\sigma}^f(\mathbf{v},p)\cdot\boldsymbol{n}_\Sigma-[\![\boldsymbol{\sigma}(\mathbf{v},p)\cdot\boldsymbol{n}]\!]_\Sigma$$

which included in Eq. (39) gives:

$$\begin{aligned}I_\Sigma&=\int_\Sigma\boldsymbol{\sigma}^f(\mathbf{v},p)\cdot\boldsymbol{n}_\Sigma\cdot[\![\mathbf{v}]\!]_\Sigma\,\mathrm{d}s+\int_\Sigma[\![\boldsymbol{\sigma}(\mathbf{v},p)\cdot\boldsymbol{n}]\!]_\Sigma\cdot(\overline{\mathbf{v}}_\Sigma-[\![\mathbf{v}]\!]_\Sigma)\,\mathrm{d}s\\&=\int_\Sigma\boldsymbol{\sigma}^f(\mathbf{v},p)\cdot\boldsymbol{n}_\Sigma\cdot[\![\mathbf{v}]\!]_\Sigma\,\mathrm{d}s+\int_\Sigma[\![\boldsymbol{\sigma}(\mathbf{v},p)\cdot\boldsymbol{n}]\!]_\Sigma\cdot\mathbf{v}_\Sigma^p\,\mathrm{d}s.\end{aligned}\tag{40}$$

By incorporating now in (40) the jump interface conditions (16) on Σ_t and noticing that the contribution of the normal component in the scalar product vanishes with $[\![\mathbf{v}\cdot\boldsymbol{n}]\!]_\Sigma=0$, it yields:

$$I_{\Sigma_t}=\frac{\mu}{\sqrt{K_p}}\sum_{j=1}^{2}\int_{\Sigma_t}\alpha_\Sigma\,[\![\mathbf{v}\cdot\boldsymbol{\tau}_j]\!]_\Sigma^2\,\mathrm{d}s+\frac{\mu}{\sqrt{K_p}}\int_{\Sigma_t}(\boldsymbol{\beta}_\Sigma\cdot\mathbf{v}_\Sigma^f)\cdot\mathbf{v}_\Sigma^p\,\mathrm{d}s,\tag{41}$$

where $(\boldsymbol{\tau}_1, \boldsymbol{\tau}_2)$ denotes a local orthonormal basis of tangential vectors on Σ. Then, the mechanical energy balance in the fluid-porous system coupled with (16) on Σ_t is finally given by Eq. (38) with (41). Since the intrinsic permeability tensor $\boldsymbol{K}_p$ is positive definite (and symmetric), all the terms in the first line of Eq. (38) are non negative. Then, considering that $\mathbf{v}^f \cdot \mathbf{v}^p \geq 0$ always holds on any interface Σ, the result below is proved.

Theorem 1 (Global dissipation of the fluid-porous models coupled on Σ_t.) *The Stokes/Darcy-Brinkman (3) and Stokes/Darcy (6) models coupled with the jump interface conditions (16) on Σ_t are both globally dissipative whatever the slip coefficient $\alpha_\Sigma \geq 0$ and the positive semi-definite friction tensor $\boldsymbol{\beta}_\Sigma \geq 0$, and the energy balance is given by Eq. (38) with (41).*

3.2 Energy balance for the fluid-porous flow with interface conditions (19) on Σ_b

Using (19) on Σ_b that involves no velocity jump at the interface with $\mathbf{v}^f_\Sigma = \mathbf{v}^p_\Sigma = \mathbf{v}_\Sigma$, the term I_Σ in Eq. (39) reduces to:

$$I_{\Sigma_b} = \frac{\mu}{\sqrt{K_p}} \int_{\Sigma_b} (\boldsymbol{\beta}_\Sigma \cdot \mathbf{v}_\Sigma) \cdot \mathbf{v}_\Sigma \, \mathrm{d}s. \tag{42}$$

Here, the mechanical energy balance in the fluid-porous system coupled with (19) on Σ_b is finally given by Eq. (38) with (42). Then, similarly to section 3.1 for Theorem 1, the following result is proved.

Theorem 2 (Global dissipation of the fluid-porous models coupled on Σ_b.) *The Stokes/Darcy-Brinkman (3) and Stokes/Darcy (6) models coupled with the jump interface conditions (19) on Σ_b are both globally dissipative whatever the positive semi-definite friction tensor $\boldsymbol{\beta}_\Sigma \geq 0$, and the energy balance is given by Eq. (38) with (42).*

The theorems 1 and 2 ensure the dissipation of the total energy inside the whole fluid-porous system. This has important consequences in terms of physical stability of the system. This also implies the mathematical stability, at least formally, *i.e.* if the solution is sufficiently regular to give a sense to the integrals over the interface; see Angot (2018) for a rigorous analysis. In particular, when no external force is applied to the system and thus when the right-hand side in (38) is zero, the static equilibrium state is exactly reached and stable only with a vanishing velocity. On the contrary, if $\alpha_\Sigma \geq 0$ or $\boldsymbol{\beta}_\Sigma \geq 0$ (in the sense of positive semi-definite matrix) does not hold, then there exists counterexamples such that this state can be associated to a non-zero velocity field. Therefore, the cases where $\alpha_\Sigma < 0$[4] or with a negative definite tensor $\boldsymbol{\beta}_\Sigma$ are not physically admissible. Moreover, since the governing equations (3) and (6) are linear for the non-inertial flows, it is an easy matter to show the uniqueness of any solution with Eq. (38) and (41) or (42) by considering the difference of two possible solutions.

[4] The case with $\alpha_\Sigma < 0$ in the jump interface conditions (16) on Σ_t would imply $|\mathbf{v}^p_\Sigma \cdot \boldsymbol{\tau}| > |\mathbf{v}^f_\Sigma \cdot \boldsymbol{\tau}|$ that is obviously not physically meaningful.

4 Validation and calibration for flow benchmark problems

Each set of interface conditions (16) and (19) is investigated on three benchmark flow problems at a permeable surface: the pressure-driven open channel flow (with a free boundary condition at the upper fluid surface), the Poiseuille pressure-driven channel flow (with a no-slip boundary condition at the upper fluid wall) and the Couette shear-driven plane channel flow (with no pressure gradient). For each of the latter problems, a reference solution is computed using our own numerical codes developed for the finite volume solution of the generalized Darcy-Brinkman problem (with variable porosity and permeability) over the whole fluid-porous channel. Hence, this reference solution represents the single-domain continuum model. Then, this enables us to validate the interface conditions and calibrate the related velocity slip coefficients and stress-jump friction coefficients for both the Stokes/Darcy-Brinkman and Stokes/Darcy coupled macroscale models. The calibration is performed using only the slip velocity defined as the fluid velocity of the reference solution on the top surface Σ_t of the inter-region located at $z = 0$ (figure 2). Next, by choosing the relative loss of flow rate inside the viscous boundary layer or over the whole channel as the criterion to minimize, optimal sets of jump interface conditions are obtained either on Σ_t at $z = 0$ or on the bottom surface Σ_b at $z = -d$ (figure 3) of the transition layer.

The case of the pressure-driven open channel flow is extensively studied in section 4.2. Hence, only some results are given for the pressure-driven Poiseuille flow in section 4.3 and for the shear-driven Couette flow in section 4.4 and they are shown to be very similar to those of the open channel flow. The corresponding analytical solutions are provided in Appendix C and D, respectively.

4.1 Reference solution of the single-domain continuum model

The one-domain continuum model in figure 1 is based on the volume averaged Stokes equation inside an heterogeneous porous medium, that is here the interfacial transition region Ω_{fp} with evolving heterogeneities of porosity and permeability in the context of fluid-porous flow. The derivation of this upscaled equation with the volume averaging method, first carried out completely by Ochoa-Tapia and Whitaker (1995a) after Ross (1983), is detailed in *Whitaker's book (1999)* (Whitaker 1999, Chapter 4) on the volume averaging method. A more recent derivation can be found in Valdés-Parada et al. (2007a) which also includes the local closure problem to predict the spatial variations of permeability. In the present study, we use the conservative form of this equation introduced for the purpose of the asymptotic modelling developed in (Angot et al. 2017, Eq. (7)), which is also more suitable for the numerical solution by finite volume methods. Indeed, these numerical methods easily ensure some highly desirable properties: local consistency of the fluxes and local conservativity at each finite volume. Hence, we consider the following generalized Darcy-Brinkman equation:

$$\begin{cases} \boldsymbol{\nabla}\cdot\mathbf{v} = 0 \\ -\boldsymbol{\nabla}\cdot\left(\dfrac{\mu}{\phi}\nabla\mathbf{v}\right) + \mu\boldsymbol{K}^{-1}(\phi)\cdot\mathbf{v} + \nabla p = \rho\boldsymbol{f} \end{cases} \quad \text{in } \Omega_{fp}, \tag{43}$$

where $\mathbf{v}$ denotes the filtration velocity defined as the superficial average, ϕ is the porosity and $\boldsymbol{K}$ the intrinsic permeability tensor. This equation is obviously extended in the homogeneous porous medium Ω_p with a constant porosity ϕ_p and permeability $\boldsymbol{K}_p = \boldsymbol{K}(\phi_p)$. Besides, it can be also extended in the pure fluid region Ω_f with a porosity $\phi_f = 1$ and an infinite permeability to recover the Stokes equation. Then, it is proved by Angot (1999) that this fictitious domain approach ensures the continuity of both velocity and stress vectors at the inter-region boundaries requiring no regularity assumptions on the porosity ϕ or permeability $\boldsymbol{K}(\phi)$ profiles in the interfacial transition region Ω_{fp}. In particular, it is considered Heaviside steps of porosity and permeability between the fluid and porous regions in Angot (1999); Angot et al. (1999); Khadra et al. (2000).

Therefore, we use Eqs. (43) in the whole fluid-porous plane channel shown in figure 8 for the further numerical experiments. For example, let us introduce the setting to make the quantities dimensionless in the case of a 1-D pressure-driven flow with no external force $\boldsymbol{f} = 0$ and an isotropic homogeneous porous medium. The fluid-porous upper interface Σ_t is located at $z = 0$ as shown in figure 2 and we choose the height H of the fluid layer, where the streamwise velocity $u(z = H) = u_m$ is maximum for the open channel flow, as the reference macroscopic length scale. To simulate numerically a semi-infinite porous layer, the heigth H_p of the porous layer should be larger than the thickness of Brinkman's viscous boundary layer. In practice, choosing $H_p = 20\,\ell$ is sufficient where ℓ is the size of the representative unit cell. We also take the characteristic velocity V based on the pressure gradient and defined by:

$$V := -\frac{H^2}{\mu}\frac{\mathrm{d}p}{\mathrm{d}x} > 0. \tag{44}$$

This choice allows us to solve the pressure-driven flows within the same unified manner and to compare more easily the results of the open channel flow (with a Neuman free boundary condition at the upper fluid surface) and the Poiseuille channel flow (with a no-slip condition at the upper wall). Indeed, the Poiseuille flow in section 4.3 gives very similar results as the open channel flow by choosing $2H$ for the height of the fluid layer, the maximum velocity being here close to the middle of this layer. Let us consider the dimensionless quantities below to normalize the governing equations:

$$Z := \frac{z}{H}, \qquad \ell^* := \frac{\ell}{H}, \qquad \delta := \frac{d}{H}, \qquad U := \frac{u}{V}, \qquad U_D := \frac{u_D}{V} = \mathrm{Da}, \tag{45}$$

ℓ being the size of the unit representative volume of the microstructure[5] and Da the Darcy number:

$$\mathrm{Da} := \frac{K_p}{H^2}, \qquad \widetilde{\mathrm{Da}}(\phi) := \frac{K(\phi)}{H^2}, \tag{46}$$

where u_D is the Darcy filtration velocity in the porous layer. The present dimensionless setting (44-46) also implies that the Darcy filtration velocity U_D equals the Darcy number Da. For the 1-D fully developed channel flow, the inertial term vanishes and the Navier-Stokes equations simply reduce to the Stokes equation whatever the

[5] The quantity ℓ^* is often denoted by ε in two-scale homogenization works.

Reynolds number. Then, the dimensionless generalized Darcy-Brinkman equation (43) reads:

$$-\frac{\mathrm{d}}{\mathrm{d}Z}\left(\frac{1}{\phi}\frac{\mathrm{d}U}{\mathrm{d}Z}\right)+\frac{1}{\widetilde{\mathrm{Da}}(\phi)}U=1,\qquad -H_p/H\le Z\le 1, \tag{47}$$

endowed with the boundary conditions below:

$$\begin{cases}\dfrac{\mathrm{d}U}{\mathrm{d}Z}(Z=1)=0,\\ U(Z=-H_p/H)=U_D \quad \text{where} \quad U_D=\mathrm{Da}.\end{cases} \tag{48}$$

All the results presented here are simulated for the flow across a 2-D array of in-line parallel circular cylinders using the $K(\phi)$ correlation (91) of Happel (1959). The dimensionless thickness δ_B of Brinkman's viscous boundary layer (or Brinkman's screening length) is estimated by the criterion below:

$$\frac{U(Z=-\delta_B)-U_D}{U_D}\le 10^{-3}. \tag{49}$$

Then, δ_B is taken large enough to verify (49) over the full range of porosity $0<\phi_p<1$. In practice, we have found $5\,\ell^*\le\delta_B\le 7\,\ell^*$ depending on H. More accurate estimations of δ_B are computed in Hernandez-Rodriguez et al. (2020) using pore-scale resolved numerical results for different microstructures and the corresponding correlations of $d_B/\sqrt{K_p}$ versus porosity ϕ_p are provided. The velocity solution inside the viscous boundary layer is also theoretically calculated by Angot et al. (2016) with WKB expansions of which the convergence is rigorously proved. Different transition profiles of porosity from ϕ_p to $\phi_f=1$ are investigated over the viscous boundary layer, as shown in figure 4 while figure 5 supplies the corresponding transition profiles of permeability.

The finite volume method with second-order accuracy in space (in the L^2 norm) is implemented with *Scilab Computing Software* to solve numerically the single-domain continuum model (47-48). A non-uniform mesh is used being uniform in each representative subdomains: the fluid layer, the viscous boundary layer and the extra porous bulk with a number of cells as large as 1024 in each part to assess the mesh numerical convergence. An example of streamwise velocity profiles in the viscous boundary layer is given in figures 6 and 7 (interfacial zoom) for the open channel flow with $H=20\,\ell$, $\delta_B=7\,\ell^*$, $\phi_p=0.75$ and $\mathrm{Da}=5.013\,10^{-5}$. This shows that the solutions for Heaviside step porosity transitions are far from that with smoother transitions. In particular, this is the case of the solution (in solid black line) corresponding to the pioneering approach of Neale and Nader (1974). For smoother porosity transitions, the differences on the slip velocity $U_s:=U(Z=0)$ remain noticeable: the mean value of U_s is $2.63\,10^{-2}$ with a standard deviation of $4.05\,10^{-3}$ with the data of figure 6. For the maximum velocity $U_m:=U(Z=1)$ in the fluid layer, the mean value is 0.526 with the same standard deviation of $4.05\,10^{-3}$. In the further calibration study, we assume a fifth-order polynomial porosity transition inside Brinkman's boundary layer to define the reference velocity profile U^{ref} with $U_m=0.529$ and $U_s=2.98\,10^{-2}$ still for the same data. All the set of interface conditions are then calibrated using only the slip velocity value U_s of the reference solution U^{ref}. For the mono-dimensional

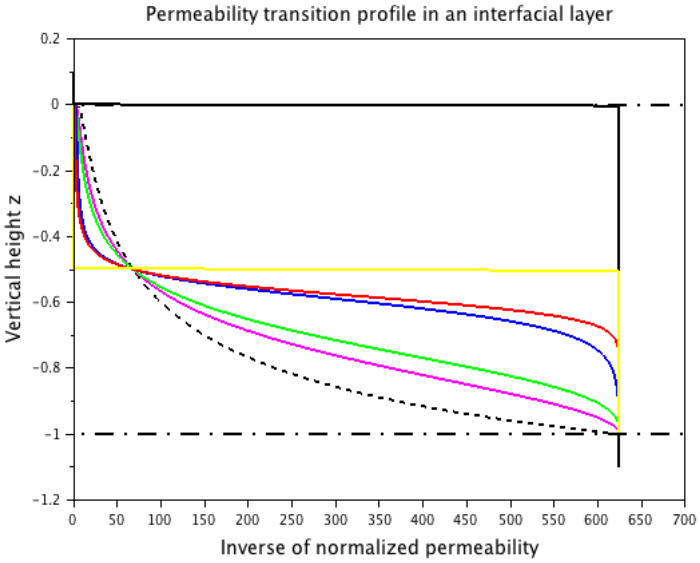

Fig. 5 Profiles of normalized inverse permeability ℓ^2/K using Eq. (91) for $K(\phi)$ correlation corresponding to the porosity transition profiles in an interfacial region Ω_{fp} shown in figure 4 (same caption).

flow, this is sufficient to get a unique solution for the Stokes/Darcy problems. For the Stokes/Darcy-Brinkman problems, there exist many possible solutions if only a single velocity value U_s is chosen to parametrize the velocity profiles. However, it is interesting to select the best solution, that is the solution which makes minimum the relative loss of volumic flow rate per unit width in the pure fluid region or in the viscous boundary layer:

$$\mathrm{er}^f = \frac{\int_0^1 |U^{ref}(z) - U(z)|\,\mathrm{d}z}{\int_0^1 U^{ref}(z)\,\mathrm{d}z}, \qquad \mathrm{er}^{bl} = \frac{\int_{-\delta_B}^0 |U^{ref}(z) - U(z)|\,\mathrm{d}z}{\int_{-\delta_B}^0 U^{ref}(z)\,\mathrm{d}z}. \tag{50}$$

The maximum relative error in the free fluid is measured by:

$$\mathrm{er}_m^f = \frac{U^{ref}(Z=1) - U(Z=1)}{U^{ref}(Z=1)}. \tag{51}$$

The error outside the interfacial region being negligible, generally $\mathrm{er}_m^f \simeq 0.092\,\%$ and $\mathrm{er}^f \simeq 0.067\,\%$, the main loss of flow rate lies in the Brinkman viscous boundary layer and er^{bl} is thus the screening criterion. However, a special attention must be paid in this optimization procedure in order to satisfy the constraint requiring that the coefficients α_Σ and β_Σ must be non negative to ensure the global dissipation of the resulting coupled macroscale problem as shown in Section 3.

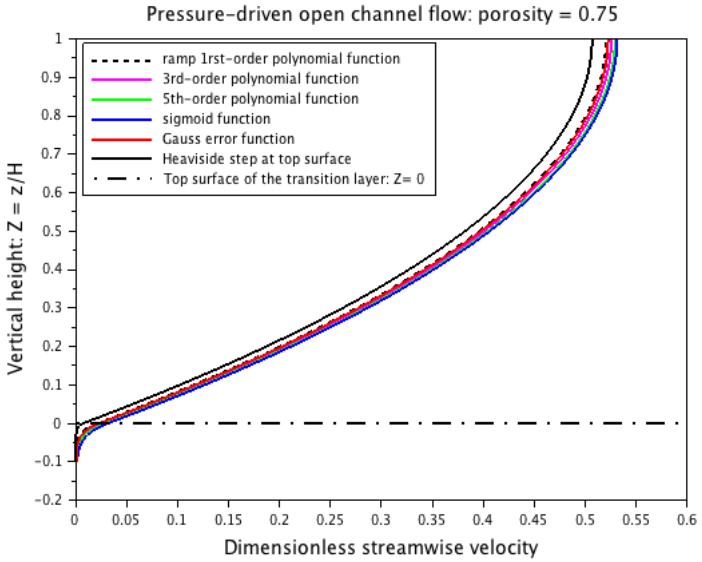

Fig. 6 Streamwise velocity solutions of the single-domain continuum model (47-48) for different porosity transition profiles (same caption as in Fig. 4) with: $H = 20\ell$, $\delta_B = 7\ell^*$, $\phi_p = 0.75$ and $\mathrm{Da} = 5.013\,10^{-5}$.

4.2 Analytical solution of the pressure-driven open channel flow

Let us consider the 1-D pressure-driven plane channel flow through a fluid layer of height H superposed to a semi-infinite layer of an isotropic and homogeneous porous medium of constant porosity ϕ_p and permeability K_p. The open channel flow is characterized by a Neumann free boundary condition at the upper surface of the fluid layer. Due to the latter condition of symmetry, this problem is equivalent to a Poiseuille flow in a pure fluid layer inserted between two horizontal porous layers. We detail below the analytical solutions of the Stokes/Darcy and Stokes/Darcy-Brinkman problems both associated with either interface conditions (16) on the top surface Σ_t of the transition layer at $Z = 0$ or (19) on the bottom surface Σ_b at $Z = -\delta$ where δ has to be determined.

4.2.1 Two solutions of the Stokes/Darcy problem

Jump interface condition (16) at Σ_t. Using (45–46), the dimensionless Stokes and Darcy governing equations read:

$$\begin{cases} \dfrac{\mathrm{d}^2 U^f}{\mathrm{d}Z^2} = -1, & 0 \le Z \le 1, \\ U^p(Z) = U_D = \mathrm{Da}, & Z \le 0, \end{cases} \tag{52}$$

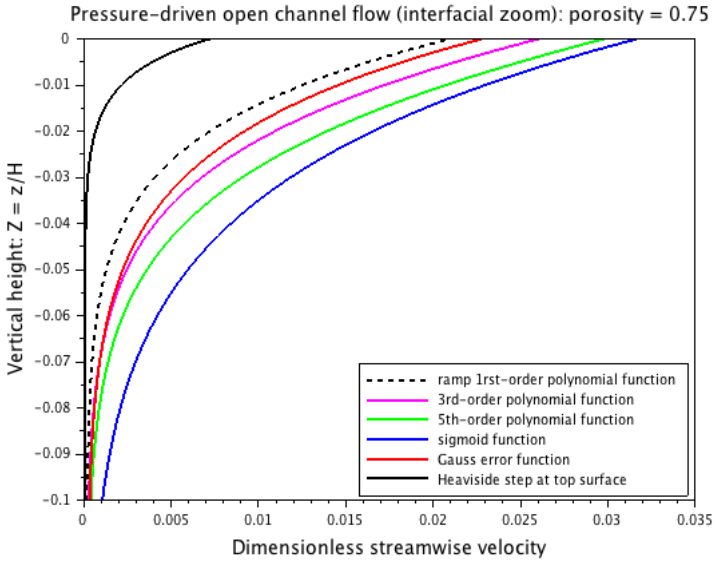

Fig. 7 Streamwise velocity solutions (interfacial zoom) of the single-domain continuum model (47-48) for different porosity transition profiles (same caption as in Fig. 4) with: $H = 20\ell$, $\delta_B = 7\ell^*$, $\phi_p = 0.75$ and $\mathrm{Da} = 5.013\,10^{-5}$.

endowed with the free-boundary or "non-friction boundary" condition at $Z = 1$:

$$\frac{\mathrm{d}U^f}{\mathrm{d}Z}(Z=1) = 0, \qquad \text{where} \qquad U^f(Z=1) = U_m, \tag{53}$$

and the interface condition (16) applied on Σ_t at $Z = 0$ which reduces for the 1-D flow to the usual Beavers-Joseph slip condition:

$$\frac{\mathrm{d}U^f}{\mathrm{d}Z}(Z=0) = 1 = \frac{\alpha_\Sigma}{\sqrt{\mathrm{Da}}}(U_s - U_D), \qquad \text{on } \Sigma = \Sigma_t \text{ at } Z = 0. \tag{54}$$

Since the maximum velocity U_m (at $Z = 1$) or the slip velocity $U_s := U^f(Z = 0)$, *i.e.* the line-averaged interfacial velocity on Σ_t, can be measured or computed in the fluid layer by relatively accurate experiments, one of these quantities can be used to parametrize the velocity profile. The solution to Eqs (52–53) yields:

$$U^f(Z) = -\frac{Z^2}{2} + Z + U_s \qquad 0 \le Z \le 1, \qquad \text{with} \qquad U_s = U_m - \frac{1}{2}. \tag{55}$$

Thus we get with (54) the calibration of α_Σ for the Stokes/Darcy problem once U_s is known from experimental or numerical data:

$$\alpha_\Sigma = \frac{\sqrt{\mathrm{Da}}}{U_s - U_D} = \frac{\sqrt{\mathrm{Da}}}{U_m - U_D - \frac{1}{2}}, \qquad \text{on } \Sigma = \Sigma_t \text{ at } Z = 0. \tag{56}$$

Jump interface condition (19) at Σ_b. Using (45–46), the dimensionless governing equations become by extending the free-fluid layer:

$$\begin{cases} \dfrac{\mathrm{d}^2 U^f}{\mathrm{d}Z^2} = -1, & -\delta \le Z \le 1, \\ U^p(Z) = U_D = \mathrm{Da}, & Z \le -\delta, \end{cases} \tag{57}$$

now endowed with the interface conditions of velocity continuity and shear stress jump (19) on Σ_b at $Z = -\delta$:

$$\begin{cases} U^f(Z=-\delta) = U^p(Z=-\delta) := U_\Sigma = U_D \\ \dfrac{\mathrm{d}U^f}{\mathrm{d}Z}(Z=-\delta) = \dfrac{\beta_\Sigma}{\sqrt{\mathrm{Da}}} U_\Sigma = \beta_\Sigma U_D \end{cases} \quad \text{on } \Sigma = \Sigma_b \text{ at } Z = -\delta, \tag{58}$$

where $\delta > 0$ and $\beta_\Sigma \ge 0$ must be determined by the calibration procedure. Then, the solution to Eqs (57–53) yields:

$$U^f(Z) = -\frac{Z^2}{2} + Z + U_s, \qquad -\delta \le Z \le 1, \quad \text{with} \quad U_s = U_m - \frac{1}{2}. \tag{59}$$

The first condition in (58) reads:

$$\delta^2 + 2\delta - 2(U_s - U_D) = 0, \tag{60}$$

which has a unique positive root $\delta^* > 0$:

$$\delta^* = -1 + \sqrt{1 + 2(U_s - U_D)} = -1 + \sqrt{2(U_m - U_D)}. \tag{61}$$

In such a channel flow when $\mathrm{Da} \ll 1$, it is clear that $U_D \ll U_m$. Thus, we have most often:

$$\delta^* \simeq \sqrt{2\,U_m} - 1 \quad \text{when} \quad U_D \ll U_m, \text{ i.e.} \quad \mathrm{Da} \ll 1. \tag{62}$$

Another good approximation of δ^* holds when $\delta^* \ll 2$ since the equation $\delta(2+\delta) = 2(U_s - U_D)$ from (60) gives:

$$\delta^* \simeq (U_s - U_D) = U_m - U_D - \frac{1}{2} \quad \text{when} \quad \delta^* \ll 2. \tag{63}$$

When Saffman's approximation holds, *i.e.* $U_D \ll U_s$ (Saffman 1971) when H is large enough, Eq. (63) shows that: $\delta^* \simeq U_s$ (within the present dimensionless setting).

Then, the second condition in (58) yields with $U_D = \mathrm{Da}$ the calibration of β_Σ for the Stokes/Darcy problem once U_s is known from experimental or numerical data:

$$\beta_\Sigma = \frac{1+\delta^*}{\sqrt{\mathrm{Da}}} = \frac{\sqrt{2(U_m - U_D)}}{\sqrt{\mathrm{Da}}}, \qquad \text{on } \Sigma = \Sigma_b \text{ at } Z = -\delta^*. \tag{64}$$

In many flow configurations when H is large enough, we have $\delta^* \ll 1$, which also means in that case $U_m \gtrsim 1/2$ with (62) or (63) such that $\delta^* \simeq U_m - 1/2$ when $\mathrm{Da} \ll 1$. It is then justified to consider the approximation below of β_Σ:

$$\beta_\Sigma^a = \frac{1}{\sqrt{\mathrm{Da}}}, \qquad \text{on } \Sigma = \Sigma_b \text{ at } Z = -\delta^* \quad \text{when} \quad \delta^* \ll 1. \tag{65}$$

It is remarkable to observe that the approximate friction coefficient β_Σ^a in (65) on Σ_b is only dependent of the microstructure of the porous medium through its permeability and of the macroscale H with the Darcy number. Both (64) and (65) are also coherent with the asymptotics: $\beta_\Sigma \to 0$ when $\mathrm{Da} \to +\infty$ and $\beta_\Sigma \to +\infty$ when $\mathrm{Da} \to 0$. Moreover, the thickness δ^* is also very few dependent on the flow configurations using (62) and $U_m \simeq 1/2$ and the relative error between (64) and (65) is:

$$\frac{\beta_\Sigma - \beta_\Sigma^a}{\beta_\Sigma^a} = \delta^*, \qquad \text{on } \Sigma = \Sigma_b \text{ at } Z = -\delta^*. \tag{66}$$

Hence, the error should be below 1% when the hypothesis $\delta^* \ll 1$ is valid, *i.e.* $d \ll H$, that is the basic assumption to derive the asymptotic interface models in Angot et al. (2017) and in the present study.

By the way, using the fact that $U_s - U_D = \delta^*(1 + \delta^*/2)$ from (60) supplies a new expression of the slip coefficient α_Σ in (56):

$$\alpha_\Sigma = \frac{\sqrt{\mathrm{Da}}}{U_s - U_D} = \frac{\sqrt{\mathrm{Da}}}{\delta^*\left(1 + \frac{\delta^*}{2}\right)}, \qquad \text{on } \Sigma = \Sigma_t \text{ at } Z = 0. \tag{67}$$

Besides when $\delta^* \ll 2$, we get with (67) the approximation below of α_Σ:

$$\alpha_\Sigma^a = \frac{\sqrt{\mathrm{Da}}}{\delta^*}, \qquad \text{on } \Sigma = \Sigma_t \text{ at } Z = 0 \quad \text{when} \quad \delta^* \ll 2. \tag{68}$$

That gives an unusual analytical expression of the slip coefficient which shows that α_Σ is largely dependent of the flow configurations since small variations of $\delta^* \simeq (U_s - U_D)$ induce significant variations on the inverse of α_Σ. This confirms, in a quantitative way, a common observation made by many authors, e.g. Larson and Higdon (1986, 1987); Sahraoui and Kaviany (1992); Alazmi and Vafai (2001); Nield (2009); Yang et al. (2017), and discussed, e.g. in Nield (2009); Jamet and Chandesris (2009); Zhang and Prosperetti (2009); Auriault (2010). In particular, the choice of Σ_t either as the tangent surface to the upper row of solid inclusions as originally suggested by Beavers and Joseph (1967) or a little bit higher in the fluid layer appears to be crucial for the calibration of Beavers-Joseph's slip coefficient α_{bj}.

The two macroscale solutions (55, 56) and (59, 61, 64) are compared in figures 8 and 9 against the reference solution U^{ref} computed with the single-domain continuum model (47, 48). In all the cases, the errors in the free fluid layer remain very small: $\mathrm{er}_m^f = 0.092\,\%$ and $\mathrm{er}^f = 0.067\,\%$. But the relative loss of flow rate in the interfacial region er^{bl} exhibits a drastic reduction of more than 55 % using the optimal stress jump condition at Σ_b giving (59, 61, 64) instead of Beavers-Joseph's slip condition at Σ_t (55, 56): er^{bl} is reduced from 97.7 % to 39.8 % for $\phi_p = 0.75$ and from 92.6 % to 39.0 % for $\phi_p = 0.95$.

In figure 10, the calibrated slip coefficient α_Σ (56) or (67) and its approximate value (68) is plotted over the full porosity range $0 < \phi_p < 1$ for different height H of the fluid layer. The re-scaled coefficient α_Σ is also plotted using (67) by changing δ^* into $(\delta^* - \ell^*/2)$ for a better comparison with usual Beavers-Joseph's coefficient α_{bj}. Indeed, the present calibration using the reference solution of the single-domain model requires to locate the top surface Σ_t of the transition layer at a distance $\ell/2$

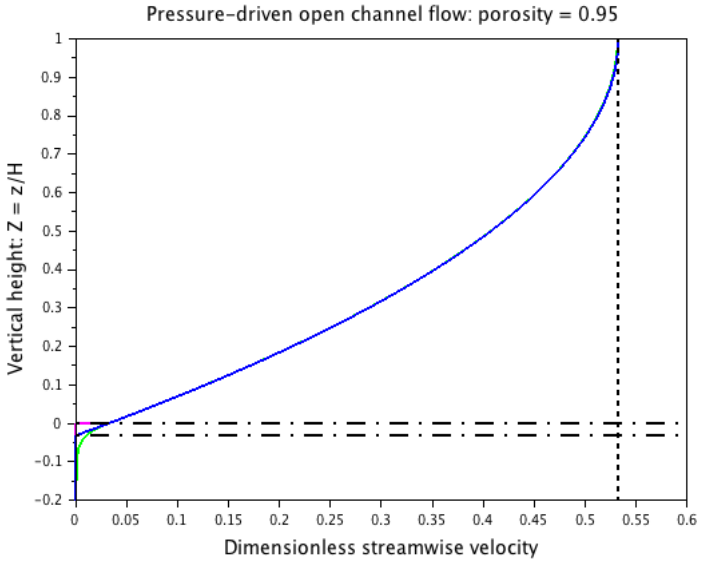

Fig. 8 Comparison of streamwise velocity solutions for the Stokes/Darcy model in the open channel flow with $H = 20\ell$, $\delta_B = 7\ell^*$, $\phi_p = 0.95$ and $\mathrm{Da} = 1.990\,10^{-4}$: general view with $U_m = 0.532$, $U_D = \mathrm{Da}$ and all solutions superposed in the fluid layer (same caption as in figure 9).

above the tangent surface of the inclusions facing the free fluid to get a porosity equal to 1 in any representative unit volume of the microstructure. The reduced slip coefficient $\alpha_\Sigma/\sqrt{\mathrm{Da}}$ is shown in figure 11 and the re-scaled value $\alpha_{\mathrm{bj}}/\sqrt{\mathrm{Da}}$ is plotted in figure 12.

In figure 13, the calibrated friction coefficient β_Σ (64) and its approximate value (65) is plotted over the full porosity range $0 < \phi_p < 1$ for different height H of the fluid layer. The reduced friction coefficient $\beta_\Sigma\sqrt{\mathrm{Da}}$ is shown in figure 14.

4.2.2 Solutions of the Stokes/Darcy-Brinkman problem

It is convenient to introduce the Brinkman number Br as the ratio of the orders of magnitude of Brinkman's viscous term over Darcy's drag, as defined in (5).

Jump interface condition (16) at Σ_t. Using (45–46), the dimensionless Stokes/Darcy-Brinkman coupled problem reads:

$$\begin{cases} \dfrac{\mathrm{d}^2U^f}{\mathrm{d}Z^2} = -1, & 0 \le Z \le 1, \\ \dfrac{1}{\phi_p}\dfrac{\mathrm{d}^2U^p}{\mathrm{d}Z^2} - \dfrac{U^p}{\mathrm{Da}} = -1, & Z \le 0, \end{cases} \tag{69}$$

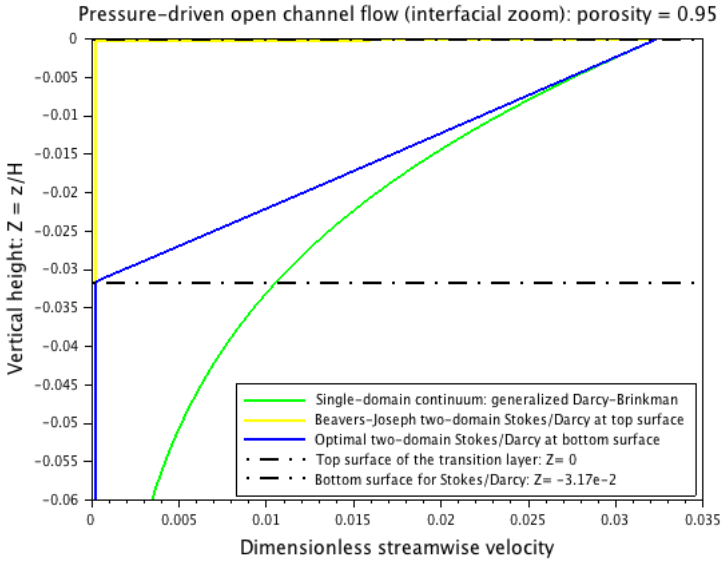

Fig. 9 Comparison of streamwise velocity solutions for the Stokes/Darcy model in the open channel flow with $H = 20\,\ell$, $\delta_B = 7\,\ell^*$, $\phi_p = 0.95$ and $\mathrm{Da} = 1.990\,10^{-4}$: interfacial region with $U_D = \mathrm{Da} = 1.990\,10^{-4}$ and $U_s = 3.24\,10^{-2}$.

endowed with the boundary conditions:

$$\begin{cases} \dfrac{\mathrm{d}U^f}{\mathrm{d}Z}(Z=1) = 0, \quad \text{where} \quad U^f(Z=1) = U_m, \\ U(Z \to -\infty) = U_D \quad \text{where} \quad U_D = \mathrm{Da}, \end{cases} \tag{70}$$

and the interface condition (16) applied on Σ_t at $Z = 0$ which reduces for the 1-D channel flow to the set:

$$\begin{cases} \dfrac{\mathrm{d}U^f}{\mathrm{d}Z}(Z=0) = \dfrac{\alpha_\Sigma}{\sqrt{\mathrm{Da}}}(U_s - U^p(Z=0)), \\ \left(\dfrac{\mathrm{d}U^f}{\mathrm{d}Z} - \dfrac{1}{\phi_p}\dfrac{\mathrm{d}U^p}{\mathrm{d}Z}\right)(Z=0) = \dfrac{\beta_\Sigma}{\sqrt{\mathrm{Da}}}U_s \end{cases} \quad \text{on } \Sigma = \Sigma_t \text{ at } Z = 0. \tag{71}$$

The solution U^f of (69, 70) in the free fluid region $0 \le Z \le 1$ is still given by (55) while the general solution U^p in the porous medium verifies:

$$U^p(Z) = A\exp(Z/\sqrt{\mathrm{Br}}) + U_D, \qquad Z \le 0, \tag{72}$$

where $A > 0$ is an adjustable constant which remains to be determined with the interface conditions (71). As expected, the Darcy filtration velocity U_D is recovered in (72) when $\mathrm{Br} \to 0$. Let us define the slip velocity U_s^p at the porous side of the dividing surface Σ_t by:

$$U_s^p := U^p(Z=0) = A + U_D. \tag{73}$$

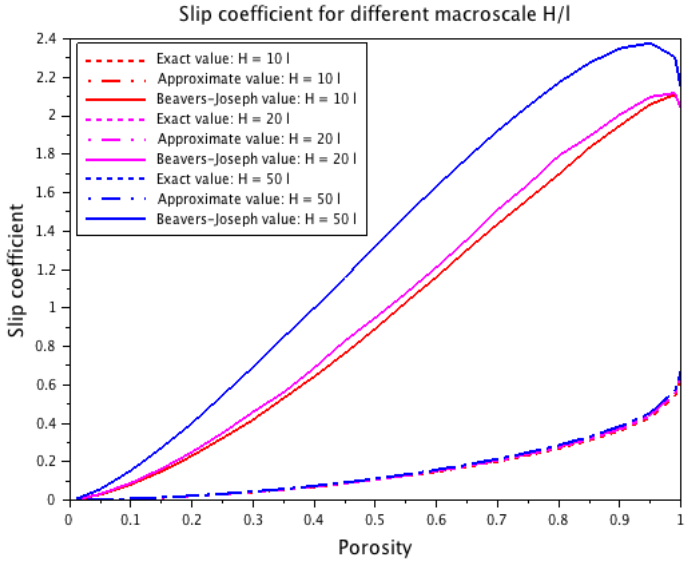

Fig. 10 Velocity slip coefficient α_Σ of the Stokes/Darcy coupled problem for the pressure-driven open channel flow with different height H of the fluid layer: $H = 10\,\ell$ (red), $H = 20\,\ell$ (magenta) and $H = 50\,\ell$ (blue) – Rescaled Beavers-Joseph's values obtained replacing δ^* by $(\delta^* - \ell^*/2)$ in Eq. (67).

Next, the physically relevance needs the non-negativity of the jump coefficients $\alpha_\Sigma \geq 0$ and $\beta_\Sigma \geq 0$ in (71) in order to satisfy the energy dissipation in the global system. We refer to Section 3.1 where the mechanical energy balance is carried out. It needs to get the velocity jump non-negative too:

$$[\![\mathbf{v}\cdot\boldsymbol{\tau}]\!]_\Sigma = (U_s - U_s^p) \geq 0, \tag{74}$$

since, if not, this would amount to a related negative value of α_Σ considering the first equation in (71). With (73), this requires:

$$0 < A \leq (U_s - U_D), \tag{75}$$

the case $A = 0$ corresponding to the Stokes/Darcy problem studied in the previous Section 4.2.1. Considering now the constraint $\beta_\Sigma \geq 0$ with the second equation in (71), this is equivalent to the inequality below:

$$A \leq \sqrt{\phi_p\,\mathrm{Da}}. \tag{76}$$

It appears that the limit case of (75), *i.e.* $A = U_s - U_D$ gives $U_s^p = U_s$ and thus $[\![\mathbf{v}\cdot\boldsymbol{\tau}]\!]_\Sigma = 0$ and velocity continuity on Σ_t whatever ϕ_p but produces $\beta_\Sigma < 0$ (using the value of U_s issued from U^{ref}). More generally, we deduce that any A such that $\sqrt{\phi_p\,\mathrm{Da}} \leq A \leq U_s - U_D$ produces $\beta_\Sigma \leq 0$. The limit case in (76) being $A = \sqrt{\phi_p\,\mathrm{Da}}$ yields $\beta_\Sigma = 0$, *i.e.* no jump of shear-stress $\boldsymbol{\tau}\cdot[\![\boldsymbol{\sigma}(\mathbf{v},p)\cdot\boldsymbol{n}]\!]_\Sigma = 0$ on Σ_t. Nevertheless, if only one point value U_s issued from the reference solution U^{ref} is used to parametrize

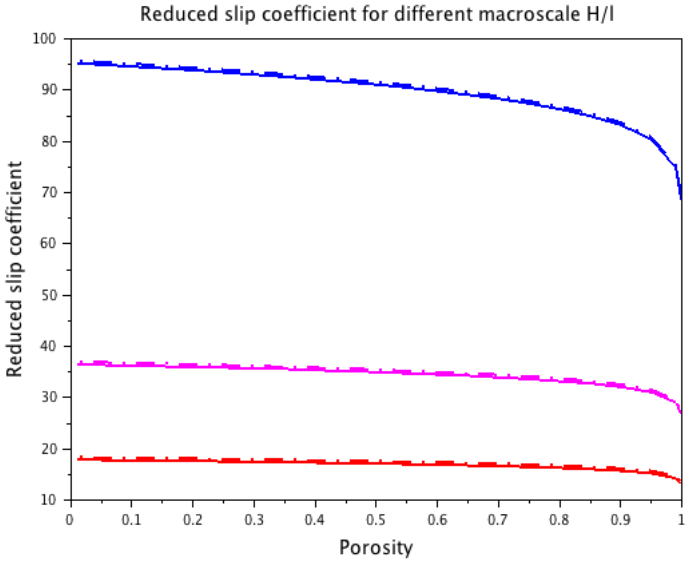

Fig. 11 Reduced slip coefficient $\alpha_\Sigma/\sqrt{\mathrm{Da}}$ of the Stokes/Darcy coupled problem for the pressure-driven open channel flow with different height H of the fluid layer: $H = 10\,\ell$ (red), $H = 20\,\ell$ (magenta) and $H = 50\,\ell$ (blue) – Exact values (solid lines) and approximate values (dashed lines).

the solution, there still exists many solutions U^p (72) satisfying the interface conditions (71) and the most strict constraint (76). Then, it is desirable to select among these solutions, the optimal one that minimizes the loss of volumic flow rate (per unit width) er^{bl} in the viscous boundary layer defined in (50). It is clear that this optimal is reached when A is maximum which also means that U_s^p is maximun. Hence the optimal solution with the interface conditions (71) on Σ_t is given by:

$$\begin{cases} U^f(Z) = -\dfrac{Z^2}{2} + Z + U_s \qquad 0 \le Z \le 1, \quad \text{with} \quad U_s = U_m - \dfrac{1}{2} \\ U^p(Z) = A\,\exp(Z/\sqrt{\mathrm{Br}}) + U_D \qquad Z \le 0, \end{cases} \tag{77}$$

with:

$$\begin{cases} A = \sqrt{\phi_p\,\mathrm{Da}}, \\ [\![U]\!]_\Sigma = U_s - U_s^p, \qquad U_s^p = \sqrt{\phi_p\,\mathrm{Da}} + U_D \\ \alpha_\Sigma = \dfrac{\sqrt{\mathrm{Da}}}{U_s - U_D - \sqrt{\phi_p\,\mathrm{Da}}}, \quad \beta_\Sigma = 0 \end{cases} \quad \text{on } \Sigma = \Sigma_t \text{ at } Z = 0. \tag{78}$$

Without further investigations for two- or three-dimensional flows with anisotropic microstructures (out the scope of the present study), it is not clear whether the property $\boldsymbol{\tau}\cdot[\![\boldsymbol{\sigma}(\mathbf{v},p)\cdot\boldsymbol{n}]\!]_\Sigma = 0$ of this optimal solution on Σ_t may be conserved or not. It is probable that such a property can be preserved among the different solutions satisfying

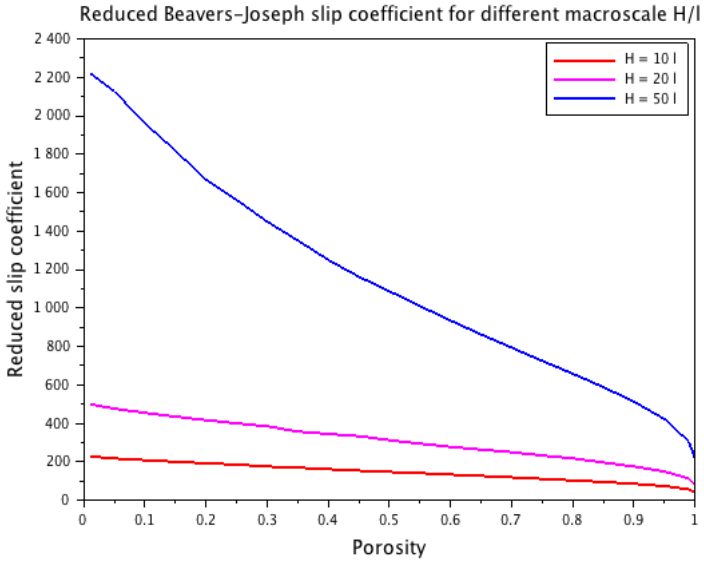

Fig. 12 Reduced Beavers-Joseph's slip coefficient $\alpha_{\rm bj}/\sqrt{\rm Da}$ of the Stokes/Darcy coupled problem for the pressure-driven open channel flow with different height H of the fluid layer: $H = 10\ell$ (red), $H = 20\ell$ (magenta) and $H = 50\ell$ (blue) – Rescaled Beavers-Joseph's values obtained replacing δ^* by $(\delta^* - \ell^*/2)$ in Eq. (67).

a positive tensor $\boldsymbol{\beta}_\Sigma \geq 0$ on Σ_t. Indeed, the anisotropic effects close to the interface should be captured by the tensorial form of $\boldsymbol{\beta}_\Sigma$ and the anisotropic intrinsic tensor of permeability $\boldsymbol{K}_p$ of the porous medium in Ω_p in the Stokes/Darcy-Brinkman problem (3).

Stress jump interface condition (19) at Σ_b. In that case, any solution satisfies now:

$$\begin{cases} U^f(Z) = -\dfrac{Z^2}{2} + Z + U_s & -\delta \leq Z \leq 1, \quad \text{with} \quad U_s = U_m - \dfrac{1}{2} \\ U^p(Z) = A\,\exp(Z/\sqrt{\rm Br}) + U_D & Z \leq -\delta, \end{cases} \tag{79}$$

where both $\delta > 0$ and $A > 0$ have now to be determined with the interface conditions (19) at Σ_b which reduce to:

$$\begin{cases} U^f(Z=-\delta) = U^p(Z=-\delta) := U_\Sigma \\ \left(\dfrac{{\rm d}U^f}{{\rm d}Z} - \dfrac{1}{\phi_p}\dfrac{{\rm d}U^p}{{\rm d}Z}\right)(Z=-\delta) = \dfrac{\beta_\Sigma}{\sqrt{\rm Da}}\,U_\Sigma \end{cases} \quad \text{on } \Sigma = \Sigma_b \text{ at } Z = -\delta, \tag{80}$$

and the constraint $\beta_\Sigma \geq 0$ to ensure the energy dissipation; see Section 3.2. Using (79) and (80), the condition $\beta_\Sigma \geq 0$ is equivalent to:

$$\begin{cases} A\,\exp(-\delta/\sqrt{\rm Br}) = (U_s - U_D) - \delta - \delta^2/2 \\ A\,\exp(-\delta/\sqrt{\rm Br}) \leq (1+\delta)\sqrt{\phi_p\,{\rm Da}}. \end{cases} \tag{81}$$

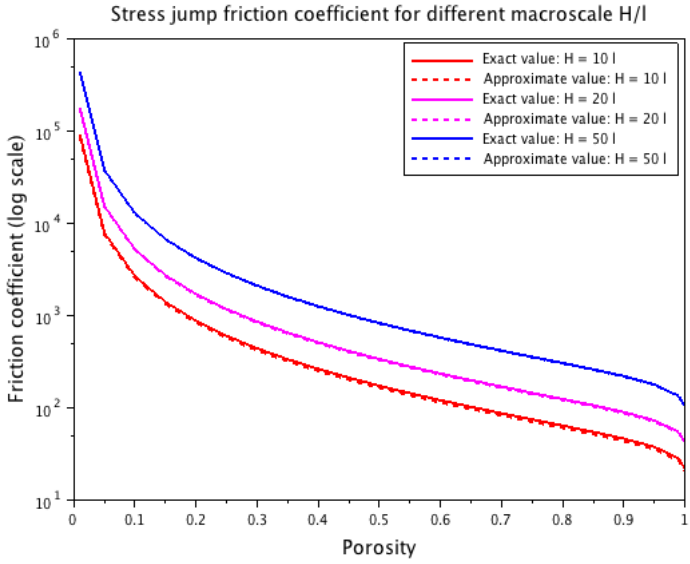

Fig. 13 Stress jump coefficient β_Σ of the Stokes/Darcy coupled problem for the pressure-driven open channel flow with different height H of the fluid layer: $H = 10\,\ell$, $H = 20\,\ell$ and $H = 50\,\ell$.

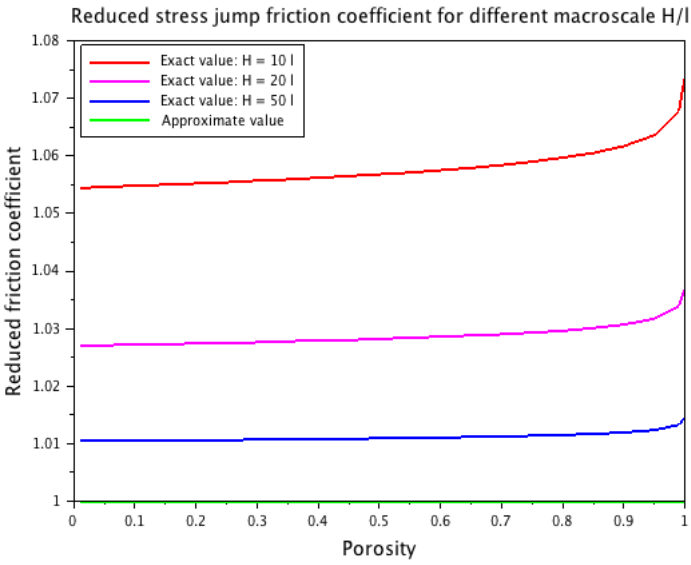

Fig. 14 Reduced friction coefficient $\beta_\Sigma \sqrt{\mathrm{Da}}$ of the Stokes/Darcy coupled problem for the pressure-driven open channel flow with different height H of the fluid layer: $H = 10\,\ell$, $H = 20\,\ell$ and $H = 50\,\ell$.

We now proceed as in the previous case on Σ_t. The limit case corresponding to $\beta_\Sigma = 0$ (related to the inflexion point in the velocity profile) in the inequality of (81) corresponds to the optimal solution minimizing the loss of flow rate er^{bl} since it makes the coefficient A maximum. Then, taking account of the first equation in (81), δ is the positive solution of the second-order equation below:

$$\delta^2 + 2\delta\,(1+\sqrt{\phi_p\,\mathrm{Da}}) + 2\,\sqrt{\phi_p\,\mathrm{Da}} - 2(U_s - U_D) = 0. \tag{82}$$

Then, as soon as U_s is known from experimental or numerical data, the unique optimal solution in this case is defined by (79) with:

$$\begin{cases} \delta^\star = -(1+\sqrt{\phi_p\,\mathrm{Da}}) + \sqrt{1+\phi_p\,\mathrm{Da} + 2(U_s - U_D)}, \\ A^\star = (1+\delta^\star)\,\sqrt{\phi_p\,\mathrm{Da}}\,\exp(\delta^\star/\sqrt{\mathrm{Br}}), \\ \beta_\Sigma^\star = 0 \end{cases} \quad \text{on } \Sigma = \Sigma_b^\star \text{ at } Z = -\delta^\star. \tag{83}$$

Therefore, $\delta^\star$ is the minimum positive value of $\delta > 0$ which ensures that the interface condition (80) is satisfied with $\beta_\Sigma \geq 0$. Moreover, by comparing (82) and (60), we get:

$$\delta^\star(2+\delta^\star) = \delta^*(2+\delta^*) - 2(1+\delta^\star)\,\phi_p\,\sqrt{\mathrm{Br}}. \tag{84}$$

This shows that $0 < \delta^\star < \delta^*$ and that $\delta^\star \longrightarrow \delta^*$ when $\mathrm{Br} \longrightarrow 0$, *i.e.* when the Stokes/Darcy-Brinkman problem reduces to the Stokes/Darcy model, that brings coherency in the present calibration approach.

Let us give another possible solution of (81) with $\beta_\Sigma > 0$ associated to the solution defined by (78) on Σ_t and verifying $U^p(Z = -\delta) = U_s^p$ given in (78). Then, δ is the positive solution of the second-order equation below:

$$\delta^2 + 2\delta + 2\,\sqrt{\phi_p\,\mathrm{Da}} - 2(U_s - U_D) = 0. \tag{85}$$

Hence, we get the solution defined by (79) with:

$$\begin{cases} \delta = -1 + \sqrt{1 + 2(U_s - U_D - \sqrt{\phi_p\,\mathrm{Da}})}, \\ A = \sqrt{\phi_p\,\mathrm{Da}}\,\exp(\delta/\sqrt{\mathrm{Br}}), \\ \beta_\Sigma = \dfrac{\delta}{\sqrt{\phi_p} + \sqrt{\mathrm{Da}}} = \dfrac{\delta}{\sqrt{\phi_p}\,(1+\sqrt{\mathrm{Br}})} \end{cases} \quad \text{on } \Sigma = \Sigma_b \text{ at } Z = -\delta. \tag{86}$$

The solution defined by (79, 86) satisfies $\beta_\Sigma > 0$ with $\delta \simeq \delta^\star$ such that $0 < \delta^\star < \delta < \delta^*$ because we have now instead of (84):

$$\delta\,(2+\delta) = \delta^*(2+\delta^*) - 2\phi_p\,\sqrt{\mathrm{Br}}. \tag{87}$$

Hence, this solution proves to be very close to the optimal one defined by (79, 83) comparing (85) with (82) and it is nearly optimal. As in Section 4.2.1 for the Stokes/Darcy problem, considering the solution (79, 86) with (85) allows us to give

the related analytical expression below of the slip coefficient α_Σ in (78) for the Stokes/Darcy-Brinkman problem:

$$\alpha_\Sigma = \frac{\sqrt{\mathrm{Da}}}{U_s - U_D - \sqrt{\phi_p\,\mathrm{Da}}} = \frac{\sqrt{\mathrm{Da}}}{\delta\left(1+\frac{\delta}{2}\right)}, \qquad \text{on } \Sigma = \Sigma_t \text{ at } Z = 0, \tag{88}$$

where δ is now given in (86). It is remarkable that the expression (88) is exactly identical to (67), although the value of δ is not the same and has to be calibrated. This is a new result since the Stokes/Darcy-Brinkman problem is generally not associated with a velocity slip interface condition. Moreover, this relation is in good agreement with the theoretical prediction of α_Σ given in (15). Let us also notice that the theoretical prediction of β_Σ in (15) is also in good agreement with that in (86) for the Stokes/Darcy-Brinkman model. However, it is important to point out that the asymptotic theory is not adapted to predict the optimal selection of solutions versus the loss of flow rate performed here for the Stokes/Darcy-Brinkman model. Most probably, our theory only provides an average coefficient β_Σ corresponding to all possible solutions of the problem that satisfy $\beta_\Sigma \geq 0$.

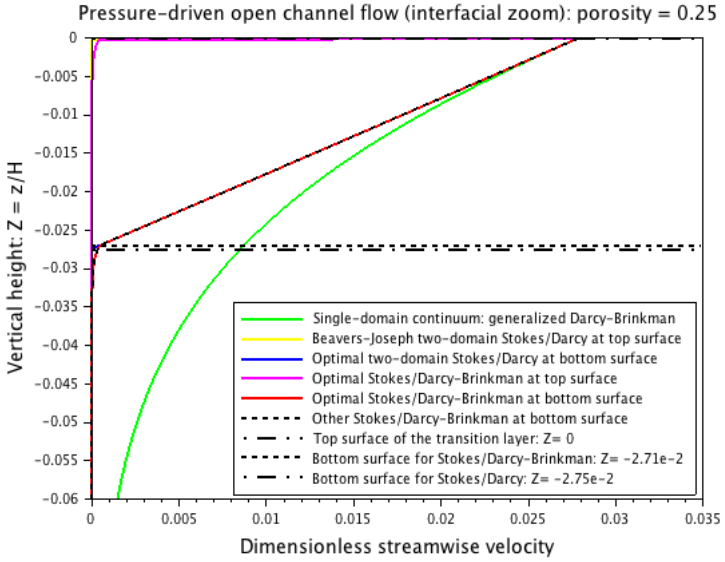

Fig. 15 Comparison of streamwise velocity solutions in the interfacial region for the Stokes/Darcy and Stokes/Darcy-Brinkman models in the open channel flow with $H = 20\,\ell$, $\delta_B = 7\,\ell^*$ and porosity $\phi_p = 0.25$: $U_D = \mathrm{Da} = 0.764\,10^{-6}$, $U_s = 2.79\,10^{-2}$ and $U_m = 0.527$.

4.2.3 Comparison and discussion

In figures 15, 16, 17 and 18, the three macroscale solutions of the Stokes/Darcy-Brinkman model (77, 78), the optimal one (79, 83) and the quasi-optimal one (79, 86)

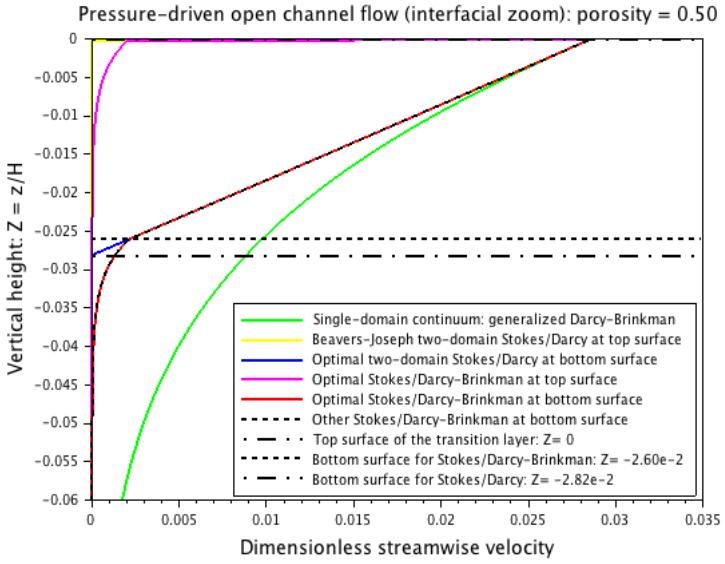

Fig. 16 Comparison of streamwise velocity solutions in the interfacial region for the Stokes/Darcy and Stokes/Darcy-Brinkman models in the open channel flow with $H = 20\,\ell$, $\delta_B = 7\,\ell^*$ and porosity $\phi_p = 0.50$: $U_D = \mathrm{Da} = 9.266\,10^{-6}$, $U_s = 2.86\,10^{-2}$ and $U_m = 0.528$.

are compared for different porosities ϕ_p with the solutions of the Stokes/Darcy model against the reference solution U^{ref} computed with the single-domain continuum model (47, 48). In all the cases, the errors in the free fluid layer remain very small: $\mathrm{er}^f_m = 0.092\,\%$ and $\mathrm{er}^f = 0.067\,\%$. However, the relative loss of flow rate in the interfacial region er^{bl} given in tables 1 and 2 exhibits a drastic reduction using the optimal stress jump condition at Σ_b leading to (83) instead of the slip condition at Σ_t verifying (78). Moreover, new expressions of the slip coefficient α_Σ are provided in Eqs. (67, 88) with respect to the thickness δ and they proved be identical for the Stokes/Darcy problem in (67) and the Stokes/Darcy-Brinkman problem in (88). This also suggests to consider the reduced coefficient $\alpha_\Sigma/\sqrt{\mathrm{Da}}$, as plotted in figures 11 and 12. The range $[0.1 - 2.4]$ of Beavers-Joseph's slip coefficient α_{bj} plotted in figure 10 within the full porosity range and for H as large as $50\,\ell$ is in agreement with the values generally calibrated in the literature using experimental or numerical results. A new general expression (64) of the friction coefficient β_Σ, plotted in figure 13, is also derived for the coupling of the Stokes/Darcy model with the stress jump interface condition (19) on Σ_b. This suggests to consider the reduced coefficient $\beta_\Sigma\sqrt{\mathrm{Da}} = 1 + \delta^*$, as plotted in figure 14 within the full range of porosity and for different macroscale lengths H/ℓ.

As a conclusion, the results shown in figures 15-18 and the related values of flow-rate's loss er^{bl} in tables 1 or 2 clearly indicate that the newly proposed stress jump interface condition (19) associated with velocity continuity on Σ_b greatly outperforms all others (16) or (17) on Σ_t for both the Stokes/Darcy-Brinkman and the Stokes/Darcy

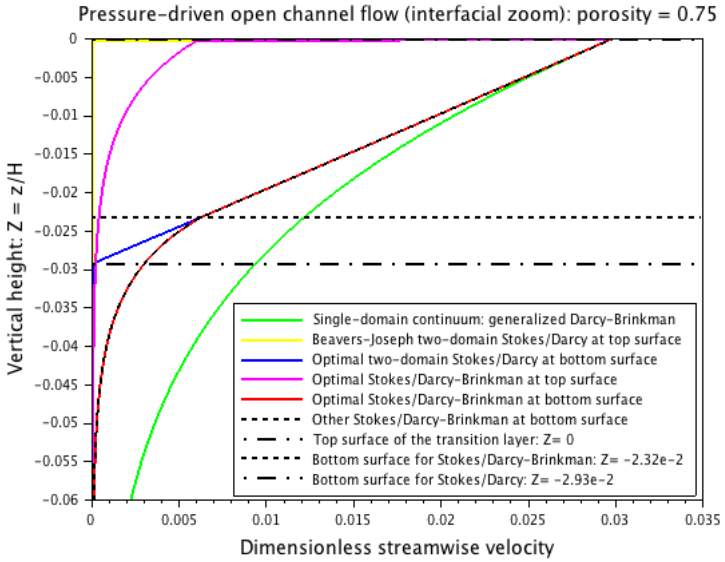

Fig. 17 Comparison of streamwise velocity solutions in the interfacial region for the Stokes/Darcy and Stokes/Darcy-Brinkman models in the open channel flow with $H = 20\,\ell$, $\delta_B = 7\,\ell^*$ and porosity $\phi_p = 0.75$: $U_D = \mathrm{Da} = 50.13\,10^{-6}$, $U_s = 2.98\,10^{-2}$ and $U_m = 0.529$.

models. In the case of the Stokes/Darcy model, it is remarkable that the stress jump interface condition (19) on Σ_b is also far better than the conditions (16) or (17) on Σ_t adjunct to the more accurate Stokes/Darcy-Brinkman model.

ϕ_p & $U_D = \mathrm{Da}$ (10^{-6})	U_s (10^{-2})	SD at Σ_t	SD at Σ_b	SDB at Σ_t	SDB at Σ_b	SDB at $\Sigma_b^\star$
0.25 & 0.764	2.79	99.9	38.7	98.3	38.003	38.001
0.50 & 9.266	2.86	99.5	39.4	96.8	37.838	37.820
0.75 & 50.13	2.98	97.7	39.8	89.9	35.044	35.005
0.95 & 199.0	3.24	92.6	39.1	71.0	27.483	27.461

Table 1 Comparative performance of the relative loss of flow rate er^{bl} (%) for the open channel flow and the different sets of interface conditions with Stokes/Darcy (SD) and Stokes/Darcy-Brinkman (SDB) models coupled with (16) at Σ_t or (19) at Σ_b: $H = 20\,\ell$ and $\delta_B = 7\,\ell^* - \mathrm{er}_m^f = 0.092\,\%$ and $\mathrm{er}^f = 0.067\,\%$.

4.3 Analytical solution of the pressure-driven Poiseuille channel flow

For the Poiseuille channel flow, all the analytical solutions of the Stokes/Darcy and Stokes/Darcy-Brinkman models coupled, either with the set of jump interface conditions (16) at Σ_t or with (19) at Σ_b, are supplied in Appendix C. As shown in figures 20 or 21 and in table 3, the comparative results with the reference solution of the

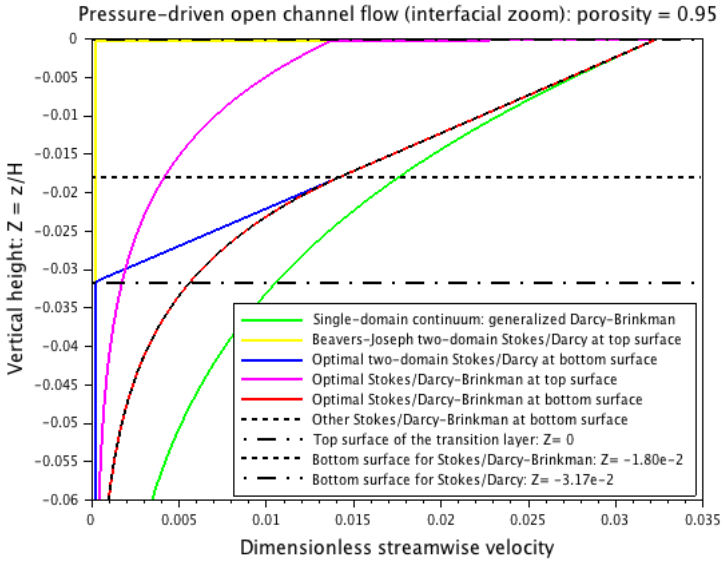

Fig. 18 Comparison of streamwise velocity solutions in the interfacial region for the Stokes/Darcy and Stokes/Darcy-Brinkman models in the open channel flow with $H = 20\,\ell$, $\delta_B = 7\,\ell^*$ and porosity $\phi_p = 0.95$: $U_D = \mathrm{Da} = 199.0\,10^{-6}$, $U_s = 3.24\,10^{-2}$ and $U_m = 0.532$.

ϕ_p & $U_D = \mathrm{Da}$ (10^{-6})	U_s (10^{-2})	SD at Σ_t	SD at Σ_b	SDB at Σ_t	SDB at Σ_b	SDB at $\Sigma_b^\star$
0.25 & 0.122	1.07	100	36.7	98.5	36.058	36.057
0.50 & 1.482	1.10	99.8	37.4	97.0	35.794	35.786
0.75 & 8.020	1.15	99.1	38.3	90.5	33.123	33.106
0.95 & 31.84	1.25	97.1	39.3	72.4	26.257	26.248

Table 2 Comparative performance of the relative loss of flow rate er^{bl} (%) for the open channel flow and the different sets of interface conditions with Stokes/Darcy (SD) and Stokes/Darcy-Brinkman (SDB) models coupled with (16) at Σ_t or (19) at Σ_b: $H = 50\,\ell$ and $\delta_B = 6\,\ell^* - \mathrm{er}_m^f = 0.096\,\%$ and $\mathrm{er}^f = 0.071\,\%$.

single-domain generalized Darcy-Brinkman model are very similar to those obtained for the open channel flow in Section 4.2. Therefore, the conclusions are the same as in Section 4.2.3.

ϕ_p & $U_D = \mathrm{Da}$ (10^{-6})	U_s (10^{-2})	SD at Σ_t	SD at Σ_b	SDB at Σ_t	SDB at Σ_b	SDB at $\Sigma_b^\star$
0.25 & 0.764	2.75	99.9	38.7	98.3	37.999	37.997
0.50 & 9.266	2.82	99.5	39.4	96.8	37.837	37.819
0.75 & 50.13	2.94	97.6	39.8	89.8	35.042	35.002
0.95 & 199.0	3.19	92.5	39.0	71.0	27.468	27.446

Table 3 Comparative performance of the relative loss of flow rate er^{bl} (%) for the Poiseuille channel flow and the different sets of interface conditions with Stokes/Darcy (SD) and Stokes/Darcy-Brinkman (SDB) models coupled with (16) at Σ_t or (19) at Σ_b: $H = 20\,\ell$ and $\delta_B = 7\,\ell^* - \mathrm{er}_m^f = 0.097\,10^{-6}$ and $\mathrm{er}^f = 0.027\,10^{-11}$.

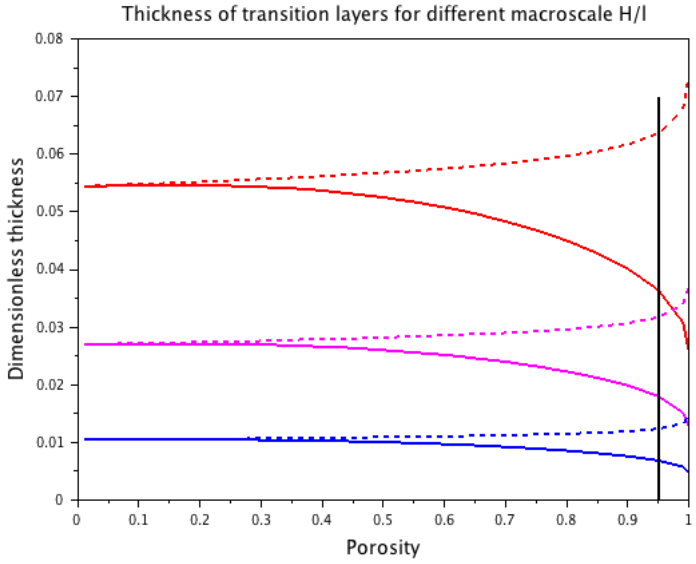

Fig. 19 Dimensionless thickness for the optimal stress jump interface conditions on Σ_b with different height H of the fluid layer: δ^* (dotted lines) for Stokes/Darcy model and $\delta^\star$ (solid lines) for Stokes/Darcy-Brinkman model – $H = 10\ell$ (red), $H = 20\ell$ (magenta) and $H = 50\ell$ (blue) – Maximum porosity limit $\phi_{max} = 0.95$ (black) for validity of Darcy's law with $H \gtrsim 20\ell$.

4.4 Analytical solution of the shear-driven Couette plane channel flow

For the Couette channel flow, all the analytical solutions of the Stokes/Darcy and Stokes/Darcy-Brinkman models coupled, either with the set of jump interface conditions (16) at Σ_t or with (19) at Σ_b, are supplied in Appendix D. As shown in figures 22 or 23 and in table 4, the comparative results with the reference solution of the single-domain generalized Darcy-Brinkman model are very similar to those obtained for the open channel flow in Section 4.2. Therefore, the conclusions are the same as in Section 4.2.3.

ϕ_p & Da (10^{-6})	U_s (10^{-2})	SD at Σ_t	SD at Σ_b	SDB at Σ_t	SDB at $\Sigma_b^\star$
0.25 & 0.764	2.38	100	33.7	99.8	33.24
0.50 & 9.266	2.45	100	34.7	98.1	32.93
0.75 & 50.13	2.57	100	36.1	90.9	30.07
0.95 & 199.0	2.83	100	38.7	71.1	23.21

Table 4 Comparative performance of the relative loss of flow rate er^{bl} (%) for the Couette channel flow and the different sets of interface conditions with Stokes/Darcy (SD) and Stokes/Darcy-Brinkman (SDB) models coupled with (16) at Σ_t or (19) at Σ_b: $H = 20\ell$ and $\delta_B = 4\ell^*$ with $U_D = 0$ – $\mathrm{er}^f = 9.00\,10^{-14}$.

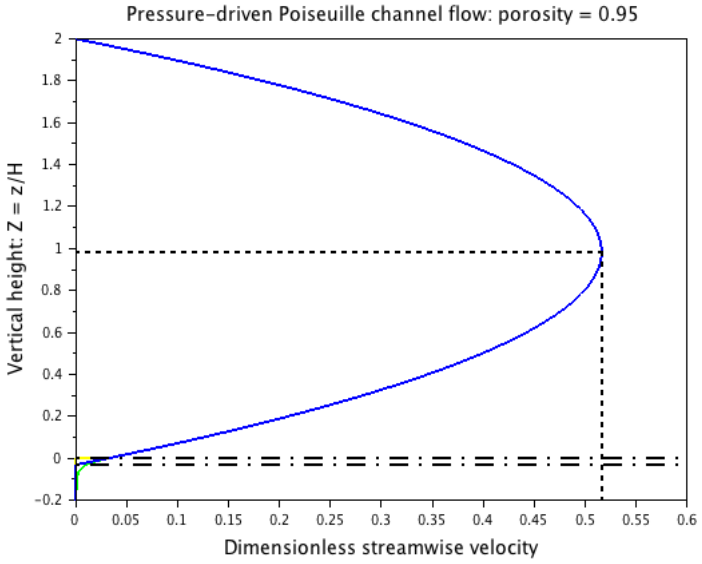

Fig. 20 Comparison of streamwise velocity solutions for the Stokes/Darcy model in the Poiseuille channel flow with $H = 20\,\ell, \delta_B = 7\,\ell^*, \phi_p = 0.95$ and $\mathrm{Da} = 1.990\,10^{-4}$: general view with $U_m = 0.516, Z_m = 0.985$, $U_D = \mathrm{Da}$ and all solutions superposed in the fluid layer (same caption as in figure 21).

4.5 Summary of the results and discussion

In the one-dimensional flows, we have shown in section 2.4 that the volume averaging and the asymptotic modelling methods produce the same interfacial model based on jump boundary conditions both for the velocity and shear stress. These jump conditions written at Σ_t or Σ_b show a good agreement with the analysis of the analytical solutions. Besides, the values of the coefficients α_Σ and β_Σ are correctly predicted by the asymptotic modelling theory in (14) or (15), except for β_Σ with the Stokes/Darcy model only. We refer to Remark 2 for a detailed explanation. In section 3, we have also shown the importance of keeping the coefficients $\alpha_\Sigma \geq 0$ and $\boldsymbol{\beta}_\Sigma \geq 0$ (as a positive semi-definite tensor) to get physically admissible solutions with respect to the dissipation of the mechanical energy. With our recent study Angot et al. (2021), this is the first time that these considerations are introduced and taken into account in the literature of fluid-porous flows.

Moreover, the main conclusions of the present calibration study are the following:

1. The sets of jump interface conditions (16) at Σ_t and (19) at Σ_b used for the coupling of both the Stokes/Darcy and Stokes/Darcy-Brinkman models share very similar results for all the three flow benchmarks: pressure-driven open or Poiseuille channel flow and shear-driven Couette channel flow.
2. The proposed set (19) at Σ_b for the coupling of either Stokes/Darcy or Stokes/Darcy-Brinkman problems is clearly far better to minimize the loss of flow rate than any suitable multi-dimensional extension (16) of Beavers-Joseph's condition on Σ_t.

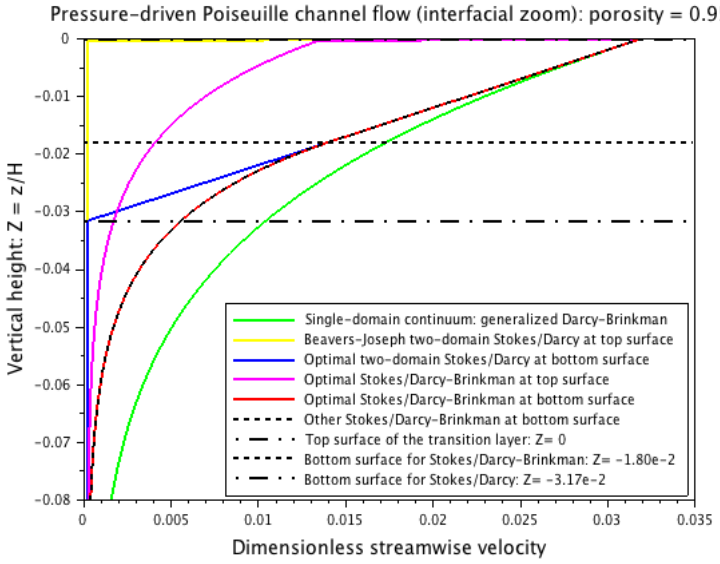

Fig. 21 Comparison of streamwise velocity solutions for the Stokes/Darcy and Stokes/Darcy-Brinkman models in the Poiseuille channel flow with $H = 20\,\ell$, $\delta_B = 7\,\ell^*$, $\phi_p = 0.95$ and $\mathrm{Da} = 1.990\,10^{-4}$: interfacial region with $U_D = \mathrm{Da} = 1.990\,10^{-4}$ and $U_s = 3.19\,10^{-2}$, $\delta^* = 3.17\,10^{-2}$, $\delta^\star = 1.80\,10^{-2}$.

This property is already true for 1-D flows and this should be conserved for multi-dimensional flows whatever direction.

3. The optimal thickness δ^* for Stokes/Darcy problems satisfies $\delta^* \gtrsim \ell^*/2$. Moreover in the present dimensionless setting, we have: $\delta^* \simeq U_s$ when H is large enough, and thus U_s appears to be a good approximate value of the required thickness δ^* in many cases; see Eqs (63), (100, 101) or (122).
4. The optimal thickness $\delta^\star$ for Stokes/Darcy-Brinkman problems satisfies whatever ϕ_p: $0 < \delta^\star < \delta^*$ and $\delta^\star \to \delta^*$ when $\mathrm{Br} \to 0$, *i.e.* when the Stokes/Darcy-Brinkman problem reduces to the Stokes/Darcy model; see (84) and figure 19. Moreover, figure 19 shows that $\delta^\star \to 0$ when $\phi_p \to 1$ and then, the set (19) reduces to continuity of velocity and stress vectors. These results show the coherency of the unified interface model proposed for the coupling of the Stokes/Darcy and Stokes/Darcy-Brinkman problems covering the whole porosity range $0 < \phi_p < 1$ of the permeable medium.
5. The original expressions of the stress jump friction coefficient β_Σ derived for the pressure-driven flows, *i.e.* (64) for the open channel flow and (102) for the Poiseuille flow, are very similar. Besides in many cases when H is large enough, they can be accurately approximated by the same value $1/\sqrt{\mathrm{Da}}$ independent of the thickness δ^*, as observed in (65) and (103); see also figures 13 and 14.

Finally, an interesting practical result can be drawn from this study for the simulation of applications at large macroscales H. In that case, the Stokes/Darcy model is the physically relevant one as indicated by figure 24. Then as shown in figures 14 and

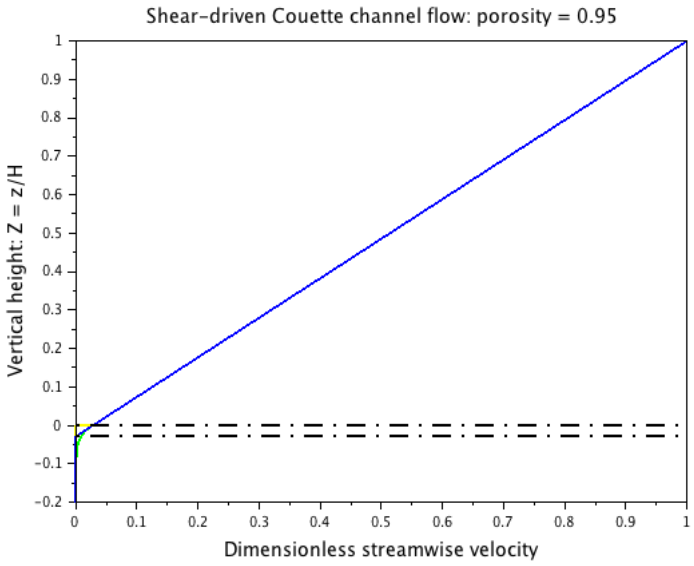

Fig. 22 Comparison of streamwise velocity solutions for the Stokes/Darcy model in the Couette channel flow with $H = 20\,\ell$, $\delta_B = 4\,\ell^*$, $\phi_p = 0.95$ and Da = $1.990\,10^{-4}$: general view with $U_m = 1$, $U_D = 0$ and all solutions superposed in the fluid layer (same caption as in figure 23).

19, using the stress jump interface condition (19) on Σ_b with $\beta_\Sigma \simeq 1/\sqrt{\mathrm{Da}}$ provides a very good approximation (all the more accurate than H is large since δ^* is all the smaller), at least for the isotropic case; see (65, 66) for the open channel flow or (103) for the Poiseuille channel flow.

5 Summary and concluding remarks

The present study provides original advances on the two-domain modelling of the viscous creeping flow in fluid-porous systems. Using the single-domain continuum modelling obtained by the volume averaging method and the asymptotic analysis derived in Angot et al. (2017), two original sets of jump interface conditions at a permeable surface are proposed for arbitrary flow directions in a unified setting: the set (16) (or (17)) applied at Σ_t and the set (19) at Σ_b. They are shown to be valid and calibrated for the coupling of both the Stokes/Darcy and the Stokes/Darcy-Brinkman models, that cover the whole range of porosity $0 < \phi_p < 1$ of the permeable medium. The comparative calibration carried out against three pressure-driven or shear-driven flow benchmarks clearly shows that the set (19), *i.e.* velocity continuity and stress jump interface conditions at Σ_b, tremendously outperforms all the others to reduce the loss of flow rate. Moreover, the proposed procedure of optimal calibration associated with the intrinsic tensorial form of (16) or (19), while ensuring the global dissipation with $\alpha_\Sigma \geq 0$ and a positive semi-definite tensor $\boldsymbol{\beta}_\Sigma$ (possibly symmetric), can be generalized

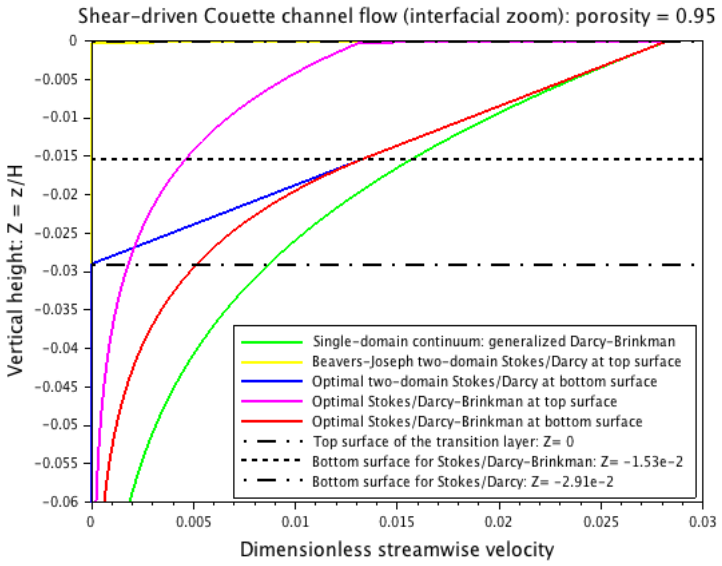

Fig. 23 Comparison of streamwise velocity solutions for the Stokes/Darcy and Stokes/Darcy-Brinkman models in the Couette channel flow with $H = 20\,\ell$, $\delta_B = 4\,\ell^*$, $\phi_p = 0.95$ and Da = $1.990\,10^{-4}$: interfacial region with $U_D = 0$ and $U_s = 2.83\,10^{-2}$, $\delta^* = 2.91\,10^{-2}$, $\delta^\star = 1.53\,10^{-2}$.

for multi-dimensional flows including anisotropic effects of the microstructure. This deserves a further study for multi-dimensional configurations with arbitrary flow directions. It is important to emphasize that the practical methodology proposed in the present study to obtain the jump boundary coefficients and the corresponding position of the dividing surface could be used with more precise expression of fluid volume fraction and permeability transition in Brinkman's viscous boundary layer Hernandez-Rodriguez et al. (2020, 2022). Finally, the set (19) is simpler to handle with numerical methods than (16) since it only involves a jump of the stress vector with no velocity jump at the interface.

Declarations

Funding

Not applicable: the authors did not receive support from any organization for the submitted work.

Conflicts of interest/Competing interests

The authors declare that they have no conflict of interest. The authors have no relevant financial or non-financial interests to disclose.

Availability of data and material

Not applicable.

Code availability

Not applicable.

Authors' contributions

All authors contributed to the study conception and design. Material preparation, data collection and analysis were performed by Philippe Angot, while discussing them with Benoît Goyeau and J. Alberto Ochoa-Tapia. The first draft of the manuscript was written by Philippe Angot and all authors commented on previous versions of the manuscript. All authors read and approved the final manuscript.

Ethics approval

Not applicable.

Consent to participate

All authors consent to participate.

Consent for publication

All authors consent for publication.

A Usual $K-\phi$ correlations for the normalized permeability

- Correlation of Kozeny-Carman Kozeny (1927), later modified by Carman (1937, 1939) and fitted to many experimental data by MacDonald et al. (1979) over a large variety of ordered or disordered media, also confirmed by MacDonald et al. (1991); Valdés-Parada et al. (2009b) for the absolute permeability of granular media composed of random packed beds of spherical particles:

$$K(\phi) \simeq \frac{d_p^2\,\phi^3}{180(1-\phi)^2}, \tag{89}$$

  where $d_p := 6\mathscr{V}_p/\mathscr{A}_p$ is the Sauter mean diameter of particles with $\mathscr{V}_p$ being the volume and $\mathscr{A}_p$ the surface area of the solid grains. It is defined as the diameter of a sphere that has the same volume/surface area ratio as a particle of interest. Using 3-D Lattice Boltzmann numerical simulations with Reynolds numbers $\mathrm{Re} < 120$ defined by $\mathrm{Re} := \rho\,|\mathbf{v}|\,d_p/\mu$, (Dye et al. 2013, table I, figure 6) investigate the broadest accessible range of porosity $0.30 \le \phi \le 0.60$ for log-normal sphere packs. Although the Kozeny-Carman relation is known to slightly underestimate the lower porosity values $\phi \le 0.42$ Dullien (1992), they show in their figure 6 that (89) fits reasonably well the simulated data.
- Correlation of Happel-Langmuir Happel (1959) (from Langmuir 1942), also reported and compared in (Jackson and James 1986, Eq. (1)) over a wide variety of experimental data for the flow parallel to a square array of parallel cylindrical rods:

$$K(\phi) \simeq \frac{d_f^2}{16(1-\phi)}\left(-\ln(1-\phi)-\frac{3}{2}+2(1-\phi)-\frac{(1-\phi)^2}{2}\right), \tag{90}$$

  where d_f is the mean diameter of fibers.
- Correlation of Happel (1959) for the transverse flow across a 2-D square array of parallel circular cylinders:

$$K(\phi) \simeq \frac{d_f^2}{32(1-\phi)}\left(-\ln(1-\phi)-\frac{1-(1-\phi)^2}{1+(1-\phi)^2}\right), \tag{91}$$

  where d_f is the mean diameter of fibers.

For ordered porous media, it is convenient to bypass the effects of the geometrical properties inside a representative unit cell in the porous medium of size ℓ by normalizing the permeability as $K(\phi)/\ell^2$ with:

$$\begin{cases} 1-\phi = \dfrac{\pi}{6}\left(\dfrac{d_p}{\ell}\right)^3 & \text{for packed spherical grains,} \\ 1-\phi = \dfrac{\pi}{4}\left(\dfrac{d_f}{\ell}\right)^2 & \text{for square arrays of circular cylinders.} \end{cases} \tag{92}$$

The corresponding Darcy number Da is defined with the macroscale length L by:

$$\mathrm{Da} := \frac{K(\phi)}{L^2} = \frac{K(\phi)}{\ell^2}\,\frac{\ell^2}{L^2}. \tag{93}$$

B Brinkman number Br: ratio of Brinkman's viscous term over Darcy's drag

In order to justify related approximations according to the range of porosity, it is important to consider the ratio Br of the orders of magnitude between Brinkman's viscous term $\boldsymbol{\nabla}\cdot\widetilde{\mu}(\nabla\mathbf{v}+\nabla\mathbf{v}^T)$ and Darcy's drag term $\mu\boldsymbol{K}^{-1}\cdot\mathbf{v}$ in Eq. (43). With the effective viscosity $\widetilde{\mu}=\mu/\phi$ (from (Whitaker 1999, Chapter 4) or Valdés-Parada et al. (2007b)) and denoting V as a characteristic scale of velocity, the former term is of order $O(\widetilde{\mu}V/L^2)$ whereas the latter is $O(\mu V/K(\phi))$. Hence, we get the so-called Brinkman number Br as defined in (5). The graph of Br versus porosity ϕ is plotted in figure 24 for different correlations $K(\phi)$ and macroscopic length scales L/ℓ. Considering that Br is the ratio of orders of magnitude only, the maximum ratio allowing us to neglect Brinkman's viscous term in front of Darcy's drag is chosen to 10^{-3} instead of the threshold of 10^{-2} more usual in Physics. Then it appears that already for a macroscale length $L \gtrsim O(20\ell)$, it is fully justified to neglect the Brinkman viscous term within the porosity range $0<\phi_p\le 0.95$ in the Darcy-Brinkman equation (3) in Ω_p which becomes the usual Darcy's law (6) for the creeping flow in Ω_p.

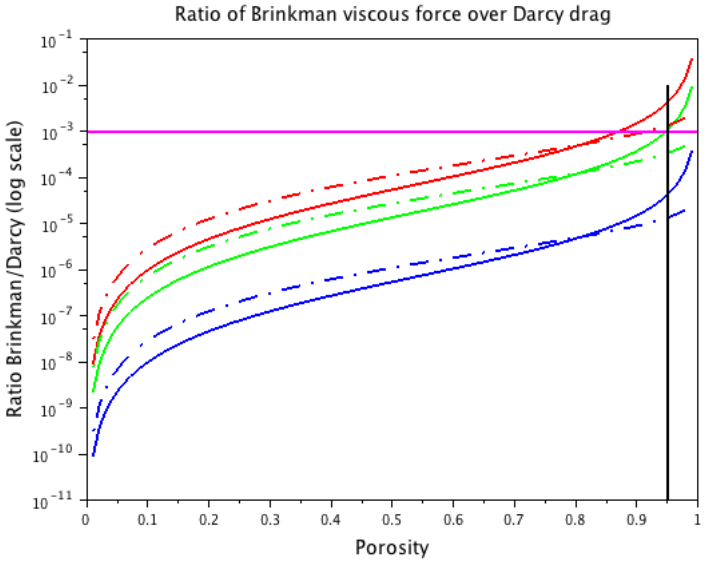

Fig. 24 Brinkman number Br as the ratio of Brinkman's viscous term over Darcy's drag (5) for different correlations $K(\phi)$ and scalings L/ℓ: Kozeny-Carman Eq. (89) (solid line) or Happel-Langmuir Eq. (90) (dashed line) for $L = 10\,\ell$ (red), $L = 20\,\ell$ (green), $L = 100\,\ell$ (blue) – Maximum ratio to neglect Brinkman's viscous force (magenta) – Maximum porosity limit $\phi_{max} = 0.95$ (black) for validity of Darcy's law.

C Analytical solution of the pressure-driven Poiseuille channel flow

The analytical velocity solutions of the Poiseuille channel flow over and through a permeable wall, *i.e.* with a no-slip condition at the top wall of the channel, are calculated using the same notations and dimensionless framework as in sections 4.1 and 4.2. The only difference with the case of the open channel flow is that the height of the fluid layer is here chosen to $2H$. Indeed, the maximum velocity is now located near below the middle of the channel and the solutions can be henceforth more easily compared; see Fig. 20.

C.1 Two solutions of the Stokes/Darcy problem

Jump interface condition (16) at Σ_t. The dimensionless analytical solution satisfying the no-slip condition $U^f(Z=2)=0$ at the upper wall of the channel reads:

$$\begin{cases} U^f(Z) = -\dfrac{Z^2}{2} + \left(1 - \dfrac{U_s}{2}\right) Z + U_s & 0 \le Z \le 2, \quad \text{with} \quad U_s = U^f(Z=0) \\ U^p(Z) = U_D = \mathrm{Da} & Z \le 0. \end{cases} \tag{94}$$

The maximum velocity U_m is located at $Z_m = 1 - U_s/2 < 1$ and given by:

$$U_m := U^f(Z_m) = \frac{1}{2}\left(1 + \frac{U_s}{2}\right)^2 \quad \text{at} \quad Z_m = 1 - \frac{U_s}{2}. \tag{95}$$

The interface condition (16) applied on Σ_t at $Z=0$ reduces for the 1-D flow to the usual Beavers-Joseph slip condition:

$$\frac{\mathrm{d}U^f}{\mathrm{d}Z}(Z=0) = 1 - \frac{U_s}{2} = \frac{\alpha_\Sigma}{\sqrt{\mathrm{Da}}}(U_s - U_D), \qquad \text{on } \Sigma = \Sigma_t \text{ at } Z=0. \tag{96}$$

Thus we get with (96) the calibration of α_Σ for the Stokes/Darcy problem once U_s is known from experimental or numerical data:

$$\alpha_\Sigma = \frac{\left(1-\frac{U_s}{2}\right)\sqrt{\mathrm{Da}}}{U_s - U_D} \qquad \text{on } \Sigma=\Sigma_t \text{ at } Z=0, \tag{97}$$

that is very similar to (56).

Jump interface condition (19) at Σ_b. Here, the dimensionless analytical solution reads:

$$\begin{cases} U^f(Z) = -\dfrac{Z^2}{2} + \left(1-\dfrac{U_s}{2}\right)Z + U_s & -\delta \le Z \le 2, \quad \text{with } U_s = U^f(Z=0) \\ U^p(Z) = U_D = \mathrm{Da} & Z \le -\delta, \end{cases} \tag{98}$$

now endowed with the interface conditions of velocity continuity and shear stress jump (19) on Σ_b at $Z=-\delta$:

$$\begin{cases} U^f(Z=-\delta) = U^p(Z=-\delta) := U_\Sigma = U_D \\ \dfrac{\mathrm{d}U^f}{\mathrm{d}Z}(Z=-\delta) = \dfrac{\beta_\Sigma}{\sqrt{\mathrm{Da}}}U_\Sigma = \beta_\Sigma U_D \end{cases} \qquad \text{on } \Sigma=\Sigma_b \text{ at } Z=-\delta, \tag{99}$$

where $\delta > 0$ and $\beta_\Sigma \ge 0$ must be determined by the calibration procedure. The first condition in (99) gives δ^* as the positive root of the equation below:

$$\delta^2 + 2\left(1-\frac{U_s}{2}\right)\delta - 2(U_s - U_D) = 0, \tag{100}$$

that is :

$$\delta^* = -\left(1-\frac{U_s}{2}\right) + \sqrt{\left(1-\frac{U_s}{2}\right)^2 + 2(U_s-U_D)} = -\left(1-\frac{U_s}{2}\right) + \sqrt{2(U_m-U_D)}. \tag{101}$$

Then, the second condition in (99) yields:

$$\beta_\Sigma = \frac{1-\frac{U_s}{2}+\delta^*}{\sqrt{\mathrm{Da}}} = \frac{\sqrt{2(U_m-U_D)}}{\sqrt{\mathrm{Da}}}, \qquad \text{on } \Sigma=\Sigma_b \quad \text{at } Z=-\delta^*. \tag{102}$$

It is clear that the two expressions of β_Σ in (64) and (102) are very similar and we get also a similar reliable approximation:

$$\beta_\Sigma^a = \frac{1}{\sqrt{\mathrm{Da}}}, \qquad \text{on } \Sigma=\Sigma_b \quad \text{at } Z=-\delta^* \quad \text{when} \quad \left|\delta^* - \frac{U_s}{2}\right| \ll 1. \tag{103}$$

Therefore, using (100) with (97), we get a new relation for α_Σ:

$$\alpha_\Sigma = \frac{\sqrt{\mathrm{Da}}}{\delta^*\left(1+\frac{\delta}{2-U_s}\right)} \qquad \text{on } \Sigma=\Sigma_t \text{ at } Z=0, \tag{104}$$

still reliably approximated by:

$$\alpha_\Sigma^a = \frac{\sqrt{\mathrm{Da}}}{\delta^*} \qquad \text{when} \quad \frac{\delta}{2-U_s} \ll 1. \tag{105}$$

C.2 Solutions of the Stokes/Darcy-Brinkman problem

Jump interface condition (16) at Σ_t. All the streamwise velocity solutions satisfy:

$$\begin{cases} U^f(Z) = -\dfrac{Z^2}{2} + \left(1 - \dfrac{U_s}{2}\right) Z + U_s & 0 \le Z \le 2, \quad \text{with} \quad U_s = U^f(Z=0) \\ U^p(Z) = A \exp(Z/\sqrt{\mathrm{Br}}) + U_D & Z \le 0, \end{cases} \tag{106}$$

endowed with the interface condition (16) applied on Σ_t at $Z = 0$:

$$\begin{cases} \dfrac{\mathrm{d}U^f}{\mathrm{d}Z}(Z=0) = \dfrac{\alpha_\Sigma}{\sqrt{\mathrm{Da}}}(U_s - U_s^p), \quad U_s^p := U^p(Z=0) \\ \left(\dfrac{\mathrm{d}U^f}{\mathrm{d}Z} - \dfrac{1}{\phi_p}\dfrac{\mathrm{d}U^p}{\mathrm{d}Z}\right)(Z=0) = \dfrac{\beta_\Sigma}{\sqrt{\mathrm{Da}}} U_s \end{cases} \quad \text{on } \Sigma = \Sigma_t \text{ at } Z = 0. \tag{107}$$

The parameters $A > 0$, U_s^p such that $U_D \le U_s^p \le U_s$, $\alpha_\Sigma \ge 0$ and $\beta_\Sigma \ge 0$ are determined to minimize the loss of flow rate. Therefore, we get for the optimal solution satisfying $\beta_\Sigma = 0$:

$$\begin{cases} A = \left(1 - \dfrac{U_s}{2}\right)\sqrt{\phi_p\,\mathrm{Da}} \\ [\![U]\!]_\Sigma = U_s - U_s^p, \qquad U_s^p = U_D + \left(1 - \dfrac{U_s}{2}\right)\sqrt{\phi_p\,\mathrm{Da}} \\ \alpha_\Sigma = \dfrac{\left(1 - \frac{U_s}{2}\right)\sqrt{\mathrm{Da}}}{U_s - U_D - \left(1 - \frac{U_s}{2}\right)\sqrt{\phi_p\,\mathrm{Da}}}, \qquad \beta_\Sigma = 0 \end{cases} \quad \text{on } \Sigma = \Sigma_t \text{ at } Z = 0. \tag{108}$$

Stress jump interface condition (19) at Σ_b. All the streamwise velocity solutions now satisfy:

$$\begin{cases} U^f(Z) = -\dfrac{Z^2}{2} + \left(1 - \dfrac{U_s}{2}\right) Z + U_s & -\delta \le Z \le 2, \quad \text{with} \quad U_s = U^f(Z=0) \\ U^p(Z) = A \exp(Z/\sqrt{\mathrm{Br}}) + U_D & Z \le -\delta, \end{cases} \tag{109}$$

endowed with the interface condition (19) applied on Σ_b at $Z = -\delta$:

$$\begin{cases} U^f(Z=-\delta) = U^p(Z=-\delta) := U_\Sigma \\ \left(\dfrac{\mathrm{d}U^f}{\mathrm{d}Z} - \dfrac{1}{\phi_p}\dfrac{\mathrm{d}U^p}{\mathrm{d}Z}\right)(Z=-\delta) = \dfrac{\beta_\Sigma}{\sqrt{\mathrm{Da}}} U_\Sigma \end{cases} \quad \text{on } \Sigma = \Sigma_b \text{ at } Z = -\delta. \tag{110}$$

The parameters $A > 0$, $\delta > 0$ and $\beta_\Sigma \ge 0$ are determined to minimize the loss of flow rate. Therefore, $\delta^\star$ is the minimum positive value of $\delta > 0$ which ensures that the interface condition (110) is satisfied with $\beta_\Sigma \ge 0$. Then, $\delta^\star$ is the positive solution of the equation below:

$$\delta^2 + 2\delta\left(1 - \frac{U_s}{2} + \sqrt{\phi_p\,\mathrm{Da}}\right) + 2\left(1 - \frac{U_s}{2}\right)\sqrt{\phi_p\,\mathrm{Da}} - 2(U_s - U_D) = 0. \tag{111}$$

This yields the unique optimal solution defined by (109, 110) associated to $\beta_\Sigma = 0$ with:

$$\begin{cases} \delta^\star = -\left(1 - \dfrac{U_s}{2} + \sqrt{\phi_p\,\mathrm{Da}}\right) + \sqrt{\left(1 - \dfrac{U_s}{2}\right)^2 + \phi_p\,\mathrm{Da} + 2(U_s - U_D)} \\ A^\star = \left(1 - \dfrac{U_s}{2} + \delta^\star\right)\sqrt{\phi_p\,\mathrm{Da}}\exp(\delta^\star/\sqrt{\mathrm{Br}}) \\ \beta_\Sigma^\star = 0 \end{cases} \quad \text{on } \Sigma = \Sigma_b^\star \text{ at } Z = -\delta^\star. \tag{112}$$

Let us give a nearly optimal solution of (109, 110) with $\beta_\Sigma > 0$ associated to the solution defined by (108) on Σ_t and verifying $U^p(Z=-\delta) = U_s^p$ given in (108). Then, δ is the positive solution of the second-order equation below:

$$\delta^2 + 2\left(1-\frac{U_s}{2}\right)\delta + 2\left(1-\frac{U_s}{2}\right)\sqrt{\phi_p\,\mathrm{Da}} - 2(U_s - U_D) = 0. \tag{113}$$

Hence, we get the solution defined by (109) with:

$$\begin{cases} \delta = -\left(1-\dfrac{U_s}{2}\right) + \sqrt{\left(1-\dfrac{U_s}{2}\right)^2 - 2\left(1-\dfrac{U_s}{2}\right)\sqrt{\phi_p\,\mathrm{Da}} + 2(U_s-U_D)} \\ A = \left(1-\dfrac{U_s}{2}\right)\sqrt{\phi_p\,\mathrm{Da}}\,\exp(\delta/\sqrt{\mathrm{Br}}) \qquad \text{on } \Sigma=\Sigma_b \text{ at } Z=-\delta. \\ \beta_\Sigma = \dfrac{\delta}{\left(1-\frac{U_s}{2}\right)\sqrt{\phi_p}+\sqrt{\mathrm{Da}}} = \dfrac{\delta}{\sqrt{\phi_p}\left(1-\frac{U_s}{2}+\sqrt{\mathrm{Br}}\right)} \end{cases} \tag{114}$$

As for the open channel flow in section 4.2, the solution defined by (109, 114) satisfies $\beta_\Sigma > 0$ with $\delta \simeq \delta^\star$ such that $0 < \delta^\star < \delta < \delta^*$ and we get that $\delta^\star \to \delta^*$ when $\mathrm{Br} \to 0$. Moreover, this allows us to give the related analytical expression below of the slip coefficient α_Σ in (108) for the Stokes/Darcy-Brinkman problem:

$$\alpha_\Sigma = \frac{\left(1-\frac{U_s}{2}\right)\sqrt{\mathrm{Da}}}{U_s - U_D - \left(1-\frac{U_s}{2}\right)\sqrt{\phi_p\,\mathrm{Da}}} = \frac{\sqrt{\mathrm{Da}}}{\delta\left(1+\frac{\delta}{2\left(1-\frac{U_s}{2}\right)}\right)} \qquad \text{on } \Sigma=\Sigma_t \text{ at } Z=0, \tag{115}$$

where δ is given in (114).

D Analytical solution of the shear-driven Couette plane channel flow

The shear-driven Couette plane channel flow is considered here through a fluid layer of height H superposed to a semi-infinite layer of an isotropic and homogeneous porous medium of constant porosity ϕ_p and permeability K_p. The fluid-porous dividing surface Σ_t is still located at $z=0$ and we choose the height H of the fluid layer where the streamwise velocity $u(z=H) = V_s$ is given and maximum as the reference macroscopic length scale. We also take the shear velocity V_s as the reference velocity. Then, we have the dimensionless quantities below to normalize the governing equations:

$$\mathrm{Da} := \frac{K_p}{H^2}, \qquad Z := \frac{z}{H}, \qquad \ell^* := \frac{\ell}{H}, \qquad \delta := \frac{d}{H}, \qquad U := \frac{u}{V_s}, \tag{116}$$

where d is the thickness of the inter-region Ω_{fp}. The Darcy filtration velocity vanishes here, *i.e.* $U_D = 0$, for the pure Couette shear-driven flow with no pressure gradient; see Fig. 22.

D.1 Two solutions of the Stokes/Darcy problem

Jump interface condition (16) at Σ_t. The solution of the Stokes/Darcy problem verifies:

$$\begin{cases} U^f(Z) = (1-U_s)Z + U_s & 0 \le Z \le 1, \quad \text{with } U^f(Z=0) := U_s,\ U^f(Z=1) := U_m = 1 \\ U^p(Z) = U_D = 0 & Z \le 0. \end{cases} \tag{117}$$

The jump interface condition (16) on Σ_t reduces to the velocity slip:

$$\frac{\mathrm{d}U^f}{\mathrm{d}Z}(Z=0) = \frac{\alpha_\Sigma}{\sqrt{\mathrm{Da}}}(U_s - U_D) = \frac{\alpha_\Sigma}{\sqrt{\mathrm{Da}}}U_s \qquad \text{on } \Sigma=\Sigma_t \text{ at } Z=0, \tag{118}$$

which provides the slip coefficient:

$$\alpha_\Sigma = \frac{1-U_s}{U_s}\sqrt{\mathrm{Da}} \qquad \text{on } \Sigma=\Sigma_t \text{ at } Z=0. \tag{119}$$

Jump interface condition (19) at Σ_b. The solution of the Stokes/Darcy problem now verifies:

$$\begin{cases} U^f(Z) = (1-U_s)Z + U_s & -\delta \le Z \le 1, \quad U^f(Z=0) := U_s,\ U^f(Z=1) := U_m = 1 \\ U^p(Z) = U_D = 0 & Z \le -\delta. \end{cases} \tag{120}$$

The jump interface condition (19) on Σ_b reads:

$$\begin{cases} U^f(Z=-\delta) = U^p(Z=-\delta) = U_D = 0 \\ \dfrac{\mathrm{d}U^f}{\mathrm{d}Z}(Z=-\delta) = \dfrac{\beta_\Sigma}{\sqrt{\mathrm{Da}}} U_D = 0 \end{cases} \quad \text{on } \Sigma = \Sigma_b \text{ at } Z = -\delta^*. \tag{121}$$

With the first equation in (121), we get:

$$\delta^* = \frac{U_s}{1-U_s}, \tag{122}$$

whereas the second one shows that β_Σ should take an infinite value on Σ_b since the shear stress in the fluid equals $(1-U_s) \neq 0$, that confirms that a single unknown is required for the calibration in 1-D, here δ^*. This allows us to give another new form of the slip coefficient using (119, 122):

$$\alpha_\Sigma = \frac{1-U_s}{U_s}\sqrt{\mathrm{Da}} = \frac{\sqrt{\mathrm{Da}}}{\delta^*} \qquad \text{on } \Sigma = \Sigma_t \text{ at } Z = 0. \tag{123}$$

D.2 Solutions of the Stokes/Darcy-Brinkman problem

Jump interface condition (16) at Σ_t. All the solutions of the Stokes/Darcy-Brinkman problem verify:

$$\begin{cases} U^f(Z) = (1-U_s)Z + U_s & 0 \le Z \le 1, \quad \text{with } U^f(Z=0) := U_s,\ U^f(Z=1) := U_m = 1 \\ U^p(Z) = A\exp(Z/\sqrt{\mathrm{Br}}) & Z \le 0, \end{cases} \tag{124}$$

supplemented with the interface condition (16) applied on Σ_t at $Z = 0$:

$$\begin{cases} \dfrac{\mathrm{d}U^f}{\mathrm{d}Z}(Z=0) = \dfrac{\alpha_\Sigma}{\sqrt{\mathrm{Da}}}(U_s - U_s^p), \quad U_s^p := U^p(Z=0) \\ \left(\dfrac{\mathrm{d}U^f}{\mathrm{d}Z} - \dfrac{1}{\phi_p}\dfrac{\mathrm{d}U^p}{\mathrm{d}Z}\right)(Z=0) = \dfrac{\beta_\Sigma}{\sqrt{\mathrm{Da}}} U_s \end{cases} \quad \text{on } \Sigma = \Sigma_t \text{ at } Z = 0. \tag{125}$$

The parameters $A > 0$, U_s^p such that $0 = U_D \le U_s^p \le U_s$, $\alpha_\Sigma \ge 0$ and $\beta_\Sigma \ge 0$ are determined to minimize the loss of flow rate. Therefore, we get for the optimal solution satisfying $\beta_\Sigma = 0$:

$$\begin{cases} A = (1-U_s)\sqrt{\phi_p\,\mathrm{Da}} & \\ [\![U]\!]_\Sigma = U_s - U_s^p, & U_s^p = (1-U_s)\sqrt{\phi_p\,\mathrm{Da}} \\ \alpha_\Sigma = \dfrac{(1-U_s)\sqrt{\mathrm{Da}}}{U_s - (1-U_s)\sqrt{\phi_p\,\mathrm{Da}}}, & \beta_\Sigma = 0 \end{cases} \quad \text{on } \Sigma = \Sigma_t \text{ at } Z = 0. \tag{126}$$

Jump interface condition (19) at Σ_b. All the solutions of the Stokes/Darcy-Brinkman problem now verify:

$$\begin{cases} U^f(Z) = (1-U_s)Z + U_s & -\delta \le Z \le 1, \quad U^f(Z=0) := U_s,\ U^f(Z=1) := U_m = 1 \\ U^p(Z) = A\exp(Z/\sqrt{\mathrm{Br}}) & Z \le -\delta, \end{cases} \tag{127}$$

supplemented with the interface condition (19) applied on Σ_b at $Z=-\delta$:

$$\begin{cases} U^f(Z=-\delta)=U^p(Z=-\delta):=U_\Sigma \\ \left(\dfrac{\mathrm{d}U^f}{\mathrm{d}Z}-\dfrac{1}{\phi_p}\dfrac{\mathrm{d}U^p}{\mathrm{d}Z}\right)(Z=-\delta)=\dfrac{\beta_\Sigma}{\sqrt{\mathrm{Da}}}U_\Sigma \end{cases} \quad \text{on } \Sigma=\Sigma_b \text{ at } Z=-\delta. \tag{128}$$

Here, the parameters $A>0$, $\delta>0$ and $\beta_\Sigma\geq 0$ are determined to minimize the loss of flow rate. Therefore, we get the optimal solution defined by (127, 128) associated to $\beta_\Sigma=0$ with:

$$\begin{cases} \delta^\star=\dfrac{U_s-(1-U_s)\sqrt{\phi_p\,\mathrm{Da}}}{1-U_s} \\ A^\star=(1-U_s)\sqrt{\phi_p\,\mathrm{Da}}\,\exp(\delta^\star/\sqrt{\mathrm{Br}}) \\ \beta_\Sigma^\star=0 \end{cases} \quad \text{on } \Sigma=\Sigma_b^\star \text{ at } Z=-\delta^\star. \tag{129}$$

This solution can be directly related to the optimal solution defined by (126) on Σ_t at $Z=0$ since we have: $U^p(Z=-\delta^\star)=U_s^p$ given in (126). Hence, this provides the related expression of the slip coefficient α_Σ in (126):

$$\alpha_\Sigma=\frac{(1-U_s)\sqrt{\mathrm{Da}}}{U_s-(1-U_s)\sqrt{\phi_p\,\mathrm{Da}}}=\frac{\sqrt{\mathrm{Da}}}{\delta^\star} \quad \text{on } \Sigma=\Sigma_t \text{ at } Z=0. \tag{130}$$

Moreover, we have: $0<\delta^\star<\delta^*$ where δ^* is given in (122) for the Stokes/Darcy problem and the coherency is respected since $\delta^\star\to\delta^*$ when $\mathrm{Br}\to 0$.

References

B. Alazmi and K. Vafai. Analysis of fluid flow and heat transfer interfacial conditions between a porous medium and a fluid layer. *Int. J. Heat Mass Transfer*, 44(9):1735–1749, 2001.

P. Angot. Analysis of singular perturbations on the Brinkman problem for fictitious domain models of viscous flows. *Math. Meth. Appl. Sci.*, 22(16):1395–1412, 1999. doi: 10.1002/(SICI)1099-1476(19991110)22:16.

P. Angot. A model of fracture for elliptic problems with flux and solution jumps. *C. R. Math. Acad. Sci. Paris Serie I*, 337(6):425–430, 2003.

P. Angot. A unified fictitious domain model for general embedded boundary conditions. *C. R. Acad. Sci. Paris*, 341(11):683–688, 2005.

P. Angot. A fictitious domain model for the Stokes/Brinkman problem with jump embedded boundary conditions. *C. R. Math. Acad. Sci. Paris*, 348(11-12):697–702, 2010.

P. Angot. On the well-posed coupling between free fluid and porous viscous flows. *Appl. Math. Lett.*, 24 (6):803–810, 2011.

P. Angot. Well-posed Stokes/Brinkman and Stokes/Darcy coupling revisited with new jump interface conditions. *ESAIM: Math. Model. and Numer. Anal.*, 52(5):1875–1911, 2018. doi: 10.1051/m2an/2017060.

P. Angot, C.-H. Bruneau, and P. Fabrie. A penalization method to take into account obstacles in incompressible viscous flows. *Numerische Mathematik*, 81(4):497–520, 1999.

P. Angot, F. Boyer, and F. Hubert. Numerical modelling of flow in fractured porous media. In F. Benkhaldoun, D. Ouazar, and S. Raghay, editors, *Finite Volumes for Complex Applications IV - Problems & perspectives*, pages 249–260. Hermes Science (London), 2005.

P. Angot, F. Boyer, and F. Hubert. Asymptotic and numerical modelling of flows in fractured porous media. *ESAIM: Math. Model. and Numer. Anal.*, 43(2):239–275, 2009.

P. Angot, G. Carbou, and V. Péron. Asymptotic study for Stokes-Brinkman model with jump embedded transmission conditions. *Asymptotic Analysis*, 96(3-4):223–249, 2016.

P. Angot, B. Goyeau, and J. A. Ochoa-Tapia. Asymptotic modeling of transport phenomena at the interface between a fluid and a porous layer: Jump conditions. *Phys. Rev. E*, 95(6):063302–(1–16), 2017.

P. Angot, B. Goyeau, and J. A. Ochoa-Tapia. A nonlinear asymptotic model for the inertial flow at a fluid-porous interface. *Adv. Water Res.*, 149(C):103798, 2021. doi: 10.1016/j.advwatres.2020.103798. (online 30 Oct. 2020).

J.-L. Auriault. About the Beavers and Joseph boundary condition. *Transp. Porous Media*, 83:257–266, 2010.

J.-L. Auriault, C. Boutin, and C. Geindreau. *Homogenization of Coupled Phenomena in Heterogeneous Media*. J. Wiley & Sons, Hoboken, 2009.

J. Barrère, O. Gipouloux, and S. Whitaker. On the closure problem for Darcy's law. *Transp. Porous Media*, 7:209–222, 1992.

G. S. Beavers and D. D. Joseph. Boundary conditions at a naturally permeable wall. *J. Fluid Mech.*, 30: 197–207, 1967.

A. Bottaro. Flow over natural or engineered surfaces: an adjoint homogenization perspective. *J. Fluid Mech. Perspectives*, 877(P1):1–91, 2019.

H. C. Brinkman. A calculation of the viscous force exerted by a flowing fluid on a dense swarm of particles. *Appl. Sci. Res.*, A1:27–34, 1947a.

H. C. Brinkman. On the permeability of media consisting of closely packed porous particles. *Appl. Sci. Res.*, A1:81–86, 1947b.

P. C. Carman. Fluid flow through a granular bed. *Trans. Inst. Chem. Eng.*, 15:150–167, 1937.

P. C. Carman. Permeability of saturated sands, soils and clays. *J. Agriculture Sci.*, 29(2):262–273, 1939.

T. Carraro, C. Goll, A. Marciniak-Czochra, and A. Mikelić. Pressure jump interface law for the Stokes-Darcy coupling: confirmation by direct numerical simulations. *J. Fluid Mech.*, 732:510–536, 2013.

T. Carraro, C. Goll, A. Marciniak-Czochra, and A. Mikelić. Effective interface conditions for the forced infiltration of a viscous fluid into a porous medium using homogenization. *Comput. Meth. Appl. Mech. Engrg.*, 292:195–220, 2015.

M. Cieszko and J. Kubik. Derivation of matching conditions at the contact surface between fluid-saturated porous solid and bulk fluid. *Transp. Porous Media*, 34:319–336, 1999.

H. Darcy. *Les fontaines publiques de la ville de Dijon*. Victor Dalmont, Paris, 1856.

F. A. I. Dullien. *Porous Media: Fluid Transport and Pore Structure*. Academic Press, New York, 2nd edition, 1992.

T. Duman and U. Shavit. An apparent interface location as a tool to solve the porous interface flow problem. *Transp. Porous Media*, 78(3):509–524, 2009.

A. L. Dye, J. E. McClure, C. T. Miller, and W. G. Gray. Description of non-Darcy flows in porous medium systems. *Phys. Rev. E*, 87(3):033012–(1–14), 2013.

E. Eggenweiler and I. Rybak. Unsuitability of the Beavers-Joseph interface condition for filtration problems. *J. Fluid Mech.*, 892:A10–(1–19), 2020.

E. Eggenweiler and I. Rybak. Effective coupling conditions for arbitrary flows in Stokes-Darcy systems. *SIAM Multiscale Model. Simul.*, 2021. arXiv:2006.12096v1 (2021, in press).

H. I. Ene and E. Sanchez-Palencia. Equations et phénomènes de surface pour l'écoulement dans un modèle de milieu poreux. *J. de Mécanique*, 14(1):73–108, 1975.

J. Finnigan. Turbulence in plant canopies. *Ann. Rev. Fluid Mech.*, 32:519–571, 2000.

B. Goyeau, D. Lhuillier, D. Gobin, and M. G. Velarde. Momentum transport at a fluid-porous interface. *Int. J. Heat Mass Transfer*, 46:4071–4081, 2003.

J. Happel. Viscous flow relative to arrays of cylinders. *AIChE J.*, 5:174–177, 1959.

R. Hernandez-Rodriguez, B. Goyeau, P. Angot, and J. A. Ochoa-Tapia. Average velocity profile between a fluid layer and a porous medium: Brinkman boundary layer. *Rev. Mexicana Ing. Química*, 19(Sup. 1): 495–520, 2020.

R. Hernandez-Rodriguez, P. Angot, B. Goyeau, and J. A. Ochoa-Tapia. Momentum transport in the free fluid-porous medium transition layer: the one-domain approach. *Chem. Eng. Sci.*, 248(A):117111, 2022. doi: 10.1016/j.ces.2021.117111. (online 20 Sept. 2021).

E. U. Hornung. In *Homogenization and porous media*, volume 6 of *Interdisciplinary Applied Mathematics*. Springer-Verlag, New York, 1997.

G. W. Jackson and D. F. James. The permeability of fibrous porous media. *Can. J. Chem. Eng.*, 64: 364–374, 1986.

W. Jäger and A. Mikelić. On the interface boundary condition of Beavers & Joseph and Saffman. *SIAM J. Appl. Math.*, 60(4):1111–1127, 2000.

W. Jäger and A. Mikelić. Modelling effective interface laws for transport phenomena between an unconfined fluid and a porous medium using homogenization. *Transp. Porous Media*, 78:489–508, 2009.

D. Jamet and M. Chandesris. On the intrinsic nature of jump coefficients at the interface between a porous medium and a free fluid. *Int. J. Heat Mass Transfer*, 52:289–300, 2009.

I. P. Jones. Low Reynolds number flow past a porous spherical shell. *Math. Proc. Cambridge Philos. Soc.*, 73(1):231–238, 1973.

K. Khadra, P. Angot, S. Parneix, and J.-P. Caltagirone. Fictitious domain approach for numerical modelling of Navier-Stokes equations. *Int. J. Numer. Meth. in Fluids*, 34(8):651–684, 2000.

D. L. Koch and R. J. Hill. Inertial effects in suspension and porous-media flows. *Ann. Rev. Fluid Mech.*, 33:619–647, 2001.

J. Kozeny. über kapillare leitung der wasser in boden. *Sitzungsber. Akad. Wiss. Wien*, 136(2a):271–306, 1927.

J. Kubik and M. Cieszko. Analysis of matching conditions at the boundary surface of a fluid-saturated porous solid and a bulk fluid: the use of lagrange multipliers. *Continuum Mech. Thermodyn.*, 17(4): 351–359, 2005.

U. Lācis, Y. Sudhakar, S. Pasche, and S. Bagheri. Transfer of mass and momentum at rough and porous surfaces. *J. Fluid Mech.*, 884:A21–(1–34), 2020.

R. E. Larson and J. J. L. Higdon. Microscopic flow near the surface of two-dimensional porous media. Part I. Axial flow. *J. Fluid Mech.*, 166:449–472, 1986.

R. E. Larson and J. J. L. Higdon. Microscopic flow near the surface of two-dimensional porous media. Part II. Transverse flow. *J. Fluid Mech.*, 178:119–136, 1987.

M. LeBars and M. G. Worster. Interfacial conditions between a pure fluid and a porous medium: implications for binary alloy solidification. *J. Fluid Mech.*, 550:149–173, 2006.

T. Lévy and E. Sanchez-Palencia. On boundary conditions for fluid flow in porous media. *Int. J. Engng Sci.*, 13(11):923–940, 1975.

T. S. Lundgren. Slow flow through stationary random beds and suspensions of spheres. *J. Fluid Mech.*, 51 (2):273–299, 1972.

I. F. MacDonald, M. S. El-Sayed, K. Mow, and F. A. L. Dullien. Flow through porous media: The Ergun equation revisited. *Ind. Ing. Chem. Fundamen.*, 18(3):199–208, 1979.

M. J. MacDonald, C. C. Chu, P. P. Guilloit, and K. M. Ng. A generalized Blake-Kozeny equation for multi-sized spherical particles. *AIChE J.*, 37:1583–1588, 1991.

M. Minale. Momentum transfer within a porous medium. I. Theoretical derivation of the momentum balance on the solid skeleton. *Phys. Fluids*, 26(12):123101, 2014a.

M. Minale. Momentum transfer within a porous medium. II. Stress boundary condition. *Phys. Fluids*, 26 (12):123102, 2014b.

A. Monti, M. Omidyeganeh, and A. Pinelli. Large-eddy simulation of an open-channel flow bounded by a semi-dense rigid filamentous canopy: scaling and flow structure. *Phys. Fluids*, 31(6):065108, 2019.

G. Neale and W. Nader. Practical significance of Brinkman's extension of Darcy's law: coupled parallel flows within a channel and a bounding porous medium. *Can. J. Chem. Engng*, 52:475–478, 1974.

H. Nepf. Flow and transport in regions with aquatic vegetation. *Ann. Rev. Fluid Mech.*, 44:123–142, 2012.

D. A. Nield. The boundary correction for the Rayleigh-Darcy problem: limitations of the Brinkman equation. *J. Fluid Mech.*, 128:37–46, 1983.

D. A. Nield. Modelling fluid flow and heat transfer in a saturated porous medium. *J. Appl. Math. Decision Sci.*, 4(2):165–173, 2000.

D. A. Nield. The Beavers-Joseph boundary condition and related matters: a historical and critical review. *Transp. Porous Media*, 78:537–540, 2009.

D. A. Nield and A. Bejan. *Convection in Porous Media*. Springer, New York, 5 edition, 2017.

J. A. Ochoa-Tapia and S. Whitaker. Momentum transfer at the boundary between a porous medium and a homogeneous fluid I: theoretical development. *Int. J. Heat Mass Transfer*, 38:2635–2646, 1995a.

J. A. Ochoa-Tapia and S. Whitaker. Momentum transfer at the boundary between a porous medium and a homogeneous fluid II: comparison with experiment. *Int. J. Heat Mass Transfer*, 38:2647–2655, 1995b.

A. Parasyris, M. Discacciati, and D. B. Das. Mathematical and numerical modelling of a circular cross-flow filtration module. *Appl. Math. Model.*, 80:84–98, 2020.

J. Prieur du Plessis and J. H. Masliyah. Mathematical modeling of flow through consolidated isotropic porous media. *Transp. Porous Media*, 3:145–161, 1988.

S. M. Ross. Theoretical model of the boundary condition at a fluid-porous interface. *AIChE J.*, 29(5): 840–846, 1983.

P. G. Saffman. On the boundary condition at the surface of a porous medium. *Stud. Appl. Math.*, 50(2): 93–101, 1971.

M. Sahraoui and M. Kaviany. Slip and no-slip velocity boundary conditions at interface of porous plain media. *Int. J. Heat Mass Transfer*, 35(4):927–943, 1992.

E. Sanchez-Palencia. *Non homogeneous media and vibration theory*, volume 127 of *Lecture Notes in Physics*. Springer-Verlag, Berlin, 1980.

E. Sanchez-Palencia. Homogenization method for the study of composite media. In F. Verhulst, editor, *Asymptotic analysis II - Surveys and New Trends*, volume 985 of *Lecture Notes in Mathematics*, pages 192–214. Springer-Verlag, Berlin, 1983.

F. J. Valdés-Parada, B. Goyeau, and J. A. Ochoa-Tapia. Jump momentum boundary condition at a fluid-porous dividing surface: derivation of the closure problem. *Chem. Engng Sci.*, 62:4025–4039, 2007a.

F. J. Valdés-Parada, J. A. Ochoa-Tapia, and J. Alvarez-Ramírez. On the effective viscosity for the Darcy-Brinkman equation. *Physica A: Stat. Mech. and its Appl.*, 385(1):69–79, 2007b.

F. J. Valdés-Parada, J. Alvarez-Ramírez, B. Goyeau, and J. A. Ochoa-Tapia. Computation of jump coefficients for momentum transfer between a porous medium and a fluid using a closed generalized transfer equation. *Transp. in Porous Media*, 78(3):439–457, 2009a.

F. J. Valdés-Parada, J. A. Ochoa-Tapia, and J. Alvarez-Ramírez. Validity of the permeability Carman-Kozeny equation: a volume averaging approach. *Physica A: Stat. Mech. and its Appl.*, 388(6):789–798, 2009b.

F. J. Valdés-Parada, C. G. Aguilar-Madera, J. A. Ochoa-Tapia, and B. Goyeau. Velocity and stress jump conditions between a porous medium and a fluid. *Adv. Water Res.*, 62:327–339, 2013.

S. Whitaker. Advances in theory of fluid motion in porous media. *Ind. Eng. Chem.*, 61(12):14–28, 1969.

S. Whitaker. Flow in porous media I: a theoretical derivation of Darcy's law. *Transp. Porous Media*, 1: 3–25, 1986.

S. Whitaker. The Forchheimer equation: a theoretical development. *Transp. Porous Media*, 25:27–61, 1996.

S. Whitaker. *The Method of Volume Averaging*, volume 13 of *Theory and Applications of Transport in Porous Media*. Kluwer Acad. Publ., Dordrecht, 1999.

K. Yang, H. Chen, and K. Vafai. Investigation of the momentum transfer conditions at the porous/free fluid interface: A benchmark solution. *Numer. Heat Transfer, Part A: Applications*, 71(6):609–625, 2017.

G. A. Zampogna and A. Bottaro. Fluid flow over and through a regular bundle of rigid fibres. *J. Fluid Mech.*, 792:5–35, 2016.

G. A. Zampogna, J. Magnaudet, and A. Bottaro. Generalized slip condition over rough surfaces. *J. Fluid Mech.*, 858:407–436, 2019.

Q. Zhang and A. Prosperetti. Pressure-driven flow in a two-dimensional channel with porous walls. *J. Fluid Mech.*, 631:1–21, 2009.